Chapter 5

Electronic Structure and Piezoelectric Properties of SbSI Crystals

Algirdas Audzijonis, Leonardas Žigas,
Raimundas Sereika and Raimundas Žaltauskas

Additional information is available at the end of the chapter

http://dx.doi.org/10.5772/64223

Abstract

The SbSI crystals are investigated in the paraelectric and ferroelectric phases. The calculations have been performed to find the symmetry and normal coordinates of vibrational modes. We have observed that potential energy with double well create the soft mode of B_{1u} symmetry in the microwave range and semisoft modes in the *IR* range. The A_u and B_g symmetry, top electronic levels of the highest valence band, are degenerate in the paraelectric phase. It is shown that the Jahn-Teller effect is caused by A_u symmetry normal mode interacting with the degenerate A_u symmetry electronic states in the valence band top. The pseudo-Jahn-Teller effect is induced due to the same mode interacting with A_u symmetry electronic states in the valence band and B_g symmetry states in the conduction band bottom. Concerning these two effects, the normal mode force constant K decreases and vibrational constants undergo changes during the phase transition. The theoretical deformation along the crystallographic—$x(\boldsymbol{a})$, $y(\boldsymbol{b})$, and $z(\boldsymbol{c})$—axes were studied for Sb atoms. The major change of piezoelectric modulus takes place in the ferroelectric phase near the phase transition temperature. At lower temperatures piezoelectric modulus changes become slow. The value as well as anomalous temperature dependence of piezoelectric modulus and $\Delta z(T)$ is influenced by the change of mean potential energy $\overline{V}_p(z)$ of Sb atoms in soft mode.

Keywords: SbSI crystals, potential energy, pseudo-Jahn-Teller effect, normal vibrational modes, piezoelectric modulus

1. Potential energy of normal vibrational modes

1.1. Introduction

SbSI has a classical ferroelectric phase (FEF) transition at the temperature $T_C = 295$ K [1, 2]. This crystal has large interest to the fundamental physical properties as well as for the promising application possibilities. It is known that it has large temperature and electric field dependence of the optical characteristics [3], electronic structure [4, 5], and other features. Petzelt [6] observed in the *IR* reflectivity spectra a strong temperature dependence of the lowest-frequency dielectric constant. Sugawara et al. [7] has determined strong temperature dependence of reflectivity for $\boldsymbol{E} \| \boldsymbol{c}$ in the range of 0–70 cm^{-1}. According to the author [7, 8], the frequencies of the soft mode are 4.0 and 6.5 cm^{-1} at temperatures 298 and 318 K in the *IR* range of SbSI spectrum. Although some authors [9] demonstrate result n (≈90%) of the frequency ≈ 9 cm^{-1} to the static dielectric constant $\varepsilon(0)$ at the room temperature, others claim the soft mode with frequency 10 cm^{-1} to be insignificant [10]. The soft mode consisting of two components has been found in the SbSI [11], SbSI-SbSeI [12], SbSI-BiSI [13], and SbSI-SbSBr systems [14] in the microwave range. The first component is a soft microwave mode bringing the major contribution in $\varepsilon(0)$, and the second is a semisoft mode in the *IR* range and contributes to $\varepsilon(0)$, which is less than 10% [15].

2. Symmetrical and normal coordinates

In [16] we have described the symmetrical and normal coordinates which were used to calculate electronic potential. As known, in the adiabatic approximation the vibration energy $E = T + V$ of a system of atoms can be expressed via normal coordinates $\boldsymbol{Q}$ as follows:

$$T = \frac{1}{2}\sum_k \left(\frac{dQ_k}{dt}\right)^2, V = \frac{1}{2}\sum_k \lambda_k Q_k^2, \tag{1}$$

The force constants λ_k are solution of the characteristic equation

$$\left|\lambda a_{ij} - b_{ij}\right| = 0 \tag{2}$$

where a_{ij} and b_{ij} are factors of the energy expression in orthogonal symmetry coordinates F_i:

$$T = \frac{1}{2}\sum_{ij} a_{ij}\frac{dF_i dF_j}{dt}, V = \frac{1}{2}\sum_{ij} b_{ij}F_i F_j. \tag{3}$$

Symmetry coordinates are defined as particular combinations of Cartesian components x_i, y_i, and z_i of displacements [17]. Similarly to the vibrations of Sb_2S_3, the ones of SbSI belong to the same irreducible representations Γ_a, since the space groups of both crystals are D_{2h}^{16} in the

http://dx.doi.org/10.5772/64223

paraelectric phase and C_{2v}^9 in the ferroelectric phase. Symmetry operations of the space group D_{2h}^{16} are $S1 \div S8$ [18, 19]. Some of them, such as S_1, S_3, S_6, and S_8, are connected with the space group C_{2v}^9. The effect of these symmetry operations is the same in the unit cell that consists of four molecules $(SbSI)_4$ as in the Sb_2S_3 unit cell [20] (**Table 1**).

Atoms Number			D_{2h}^{16}							
Rao [19]		**Balkanski [18]**	**S1**	**S2**	**S3**	**S4**	**S5**	**S 6**	**S7**	**S 8**
Sb_2S_3	**SbSI**	**SbSI**	**S1**		**S3**			**S 6**		**S 8**
							C_{2v}^9			
2	1	Sb2	Sb2	Sb4	Sb1	Sb3	Sb1	Sb3	Sb2	Sb4
3	2	S2	S2	S4	S1	S3	S1	S3	S2	S4
5	3	I4	I4	I2	I3	I1	I3	I1	I4	I2
7	4	Sb4	Sb4	Sb2	Sb3	Sb1	Sb3	Sb1	Sb4	Sb2
8	5	S4	S4	S2	S3	S1	S3	S1	S4	S2
10	6	I2	I2	I4	I1	I3	I1	I3	I2	I4
12	7	Sb1	Sb1	Sb3	Sb2	Sb4	Sb2	Sb4	Sb1	Sb3
13	8	S1	S1	S3	S2	S4	S2	S4	S1	S3
15	9	I3	I3	I1	I4	I2	I4	I2	I3	I1
17	10	Sb3	Sb3	Sb1	Sb4	Sb2	Sb4	Sb2	Sb3	Sb1
18	11	S3	S3	S1	S4	S2	S4	S2	S3	S1
20	12	I1	I1	I3	I2	I4	I2	I4	I1	I3

Table 1. Symmetry operations of the space groups D_{2h}^{16} and C_{2v}^9 in SbSI crystals.

The operator of projection is

$$\varepsilon_{ij}^{\alpha} = \frac{f_{\alpha}}{g} \sum_k \Gamma_{\alpha} \left(S_k \right)_{ij} S_k . \tag{4}$$

The Cartesian components $K_{An} = x_{An}, y_{An}, z_{An}$ of atom displacements for all their linear combinations have certain symmetry properties with respect to operations of groups D_{2h}^{16} and C_{2v}^9:

$$K_{Am}^{S} \left(\Gamma_{\alpha} \right) = \sum_m a_{nm} K_{An} . \tag{5}$$

Here A = Sb, S, I; n = 1, 2, 3, 4; $a_{nm} = \pm 1$. These combinations of K_{An} are basis functions of Γ_a.

Group D_{2h}^{16} has irreducible representations $A_{ig(u)}$, $B_{ig(u)}$. Here, the capital letters denote coordinates symmetric (A) or antisymmetric (B) with respect to all rotation C_2^z, C_2^y, and C_2^x, **Table 2** [21]. Subscripts denote the coordinates symmetric (g), or antisymmetric (u) with respect to inversion I. The coordinates symmetric with respect to separate rotations around x, y, and z axes differ from each other by index $i = 1, 2, 3$. The obtained K_{An} combinations are also the basic functions of irreducible representations A_i, B_i of the space group C_{2v}^9.

D_{2h}^{16}				S1		S2	S3	S4	S5	S6	S7	S8
				E	C_2^y	C_2^z	C_2^x	I	σ_y	σ_z	σ_x	σ
	C_{2v}^9			S1		S3			S6		S8	
r 1	A_{1g}	r 1	A1	1	1	1	1	1	1	1	1	
r 2	A_{1u}	r 2	A2	1	1	1	1	−1	−1	−1	−1	
r 3	B_{2g}	r 3	B1	1	−1	1	−1	1	−1	1	−1	
r 4	B_{2u}	r 4	B2	1	−1	1	−1	−1	1	−1	1	
r 5	B_{1g}	r 2	A2	1	1	−1	−1	1	1	−1	−1	
r 6	B_{1u}	r 1	A1	1	1	−1	−1	−1	−1	1	1	
r 7	B_{3g}	r 4	B2	1	−1	−1	1	1	−1	−1	1	
r 8	B_{3u}	r 3	B1	1	−1	−1	1	−1	1	1	−1	

Table 2. Group characters of irreducible representations of space groups D_{2h}^{16} and C_{2v}^9 [21].

Orthogonal symmetry coordinates of the entire unit cell can be formed of $K_{Am}^S(\Gamma_\alpha)$ by solving equations of orthonormality and are uniform with respect to A. Their expressions are as follows:

$$F_S\left(K,\Gamma_a\right) = N_S \sum_A \sum_m C_{ms} K_{Am}^{(S)}\left(\Gamma_\alpha\right) \tag{6}$$

Normalization factors N_s and coefficients C_n are presented in z direction and x, y directions in **Table 3** [22]. The group theoretical analysis reveals that they are the unit cell of D_{2h}^{16} point group with 12 atoms per cell and contains 33 optical modes and 3 acoustic modes. Among the optical modes, there are 18 Raman-active modes with the symmetries $6A_g + 6B_{1g} + 3B_{2g} + 3B_{3g}$, 3 silent modes belong to the A_u irreducible representation, as well as 12 infrared active modes that have symmetries $2B_{1u} + 5B_{2u} + 5B_{3u}$. In z direction, only $2B_{1u}$ modes are infrared active in the paraelectric phase (**Table 3**), whereas in the same direction, the modes $2A_1 + 3A_2 + 3B_1 + 3B_2$ are Raman active in the ferroelectric phase. Note that $2A_1 + 3B_1 + 3B_2$ are also infrared active among these modes.

Taking into account the fact that SbSI crystal is made of two double chains with a weak interaction between them at $T = 0$ K (20–30 times weaker than within a chain; see **Figure 1**), the formation of dynamical matrix 3 becomes easier.

Γ_α	S	N_S	Sb_1	Sb_2	Sb_3	Sb_4	S_1	S_2	S_3	S_4	I_1	I_2	I_3	I_4
$B_{1u}\left(D_{2h}^{16}\right)$	1	$\frac{1}{\sqrt{12}}$	+1	−1	−1	+1	+1	+1	+1	+1	+1	+1	+1	+1
$A_1\left(C_{2v}^{9}\right)$	2	$\frac{1}{\sqrt{8}}$	+1	+1	+1	+1	−1	−1	−1	−1	0	0	0	0
	3	$\frac{1}{\sqrt{24}}$	+1	+1	+1	+1	+1	+1	+1	+1	−2	−2	−2	−2
$B_{2g}\left(D_{2h}^{16}\right)$	4	$\frac{1}{\sqrt{12}}$	−1	+1	+1	−1	−1	+1	+1	−1	+1	−1	−1	+1
$B_1\left(C_{2v}^{9}\right)$	5	$\frac{1}{\sqrt{8}}$	−1	+1	+1	−1	+1	−1	−1	+1	0	0	0	0
	6	$\frac{1}{\sqrt{24}}$	−1	+1	+1	−1	−1	+1	+1	−1	−2	+2	+2	−2
$B_{3g}\left(D_{2h}^{16}\right)$	7	$\frac{1}{\sqrt{12}}$	−1	+1	−1	+1	−1	+1	−1	+1	−1	+1	−1	+1
$B_2\left(C_{2v}^{9}\right)$	8	$\frac{1}{\sqrt{8}}$	−1	+1	−1	+1	+1	−1	+1	−1	0	0	0	0
	9	$\frac{1}{\sqrt{24}}$	−1	+1	−1	+1	−1	+1	−1	+1	+2	−2	+2	−2
$A_u\left(D_{2h}^{16}\right)$	10	$\frac{1}{\sqrt{12}}$	+1	+1	−1	−1	+1	+1	−1	−1	−1	−1	+1	+1
$A_2\left(C_{2v}^{9}\right)$	11	$\frac{1}{\sqrt{8}}$	+1	+1	−1	−1	−1	−1	+1	+1	0	0	0	0
	12	$\frac{1}{\sqrt{24}}$	+1	+1	−1	−1	+1	+1	−1	−1	+2	+2	−2	−2

Table 3. Symmetry coordinates of normal modes of SbSI crystals in $z(\boldsymbol{c})$ direction.

In our research, force constants for a long chain of strongly bound atoms in the direction of $z(\boldsymbol{c})$-axis were defined by composing five simplified unit cells (30 atoms). The GAMESS program in the basis sets of atomic functions 3*G*, 3*G* + *d*, 21*G*, 21*G* + *d* were used to calculate force constants.

When atoms are vibrating, interaction between double chains strengthens. Therefore, following Furman et al. [23], we calculated normal models employing the Born-von Karman model and the elementary cell of four pseudomolecules SbSI (12 atoms). The binding constants and ionic charges, 0.19 (Sb), −0.01 (*S*), −0.18 (*I*), were also calculated. It appeared that covalent interactions prevailed in the SbSI crystal.

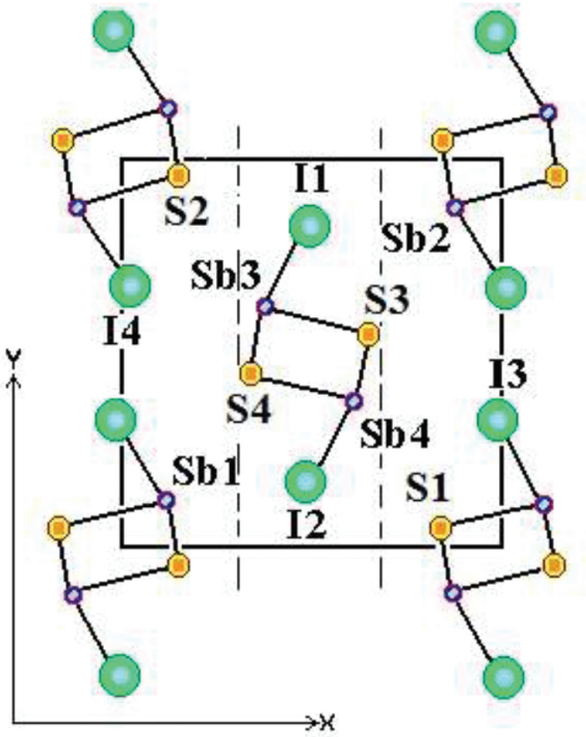

Figure 1. Locations of atoms in the unit cell of SbSI in the x–y plane. Dotted lines restrict the simplified unit cell, as formed by the central group of atoms Sb3, Sb4, S3, S4, I1, and I2.

3. The lattice anharmonism on the vibrational spectrum along the $z(c)$ direction

In [24] we have proposed the method for calculating the total potential energy. The potential energy (PE) is defined as follows:

$$V(\boldsymbol{r}) = \frac{4\pi}{\Omega}\sum_{\alpha s}|\boldsymbol{s}|^{-2} f_\alpha(\boldsymbol{s})\exp\left[-i\left(\boldsymbol{r}+\boldsymbol{R}_\alpha+\boldsymbol{Q}_\alpha\right)\cdot\boldsymbol{s}\right]\exp\left[-M_\alpha(\boldsymbol{s})\right], \tag{7}$$

where Ω stands for the volume of the unit cell, $\boldsymbol{Q}$ represents the normal coordinate, $\boldsymbol{R}_\alpha$ denotes the radius-vector of the atom position in the unit cell, $\boldsymbol{s}$ means the reciprocal lattice vector, α represents the number and kind of the atom in the unit cell, and $\exp[-M_\alpha(\boldsymbol{s})]$ represents the Debye-Valler factor that is determined by the mean square amplitudes of atomic displacements (i.e., by the crystal temperature).

In fact, Eq. (7) at a certain point in the unit cell is the PE in terms of normal coordinates (or symmetrized plane waves). The atomic scattering form factor is

$$f_\alpha(\boldsymbol{s}) = \sum_{nlm} nlm \left| \exp\left[i(\boldsymbol{r}\cdot\boldsymbol{s}) \right] nlm \right|, \tag{8}$$

where *nlm* represents a set of quantum numbers for the atom α. It is noteworthy that the functions < *nlm* of all electronic states of an atom was used for calculating the form factors f_α (***s***) by Eq. (8). About 5000 vectors ***s*** were used for the sum in Eq. (7).

For SbSI, we studied the dependence of potential energy $V(z)$ in the paraelectric phase at T = 420 K on the normal coordinates of all D_{2h}^{16} symmetry normal modes that formed by displacements of the atoms along the z direction (along the polar axis ***c***; **Figure 2**). This dependence was calculated by Eqs. (7) and (8). We determined that the curves $V(z)$ can be described by the equation

$$V(z) = V_0 + az + bz^2 + dz^3 + cz^4, \tag{9}$$

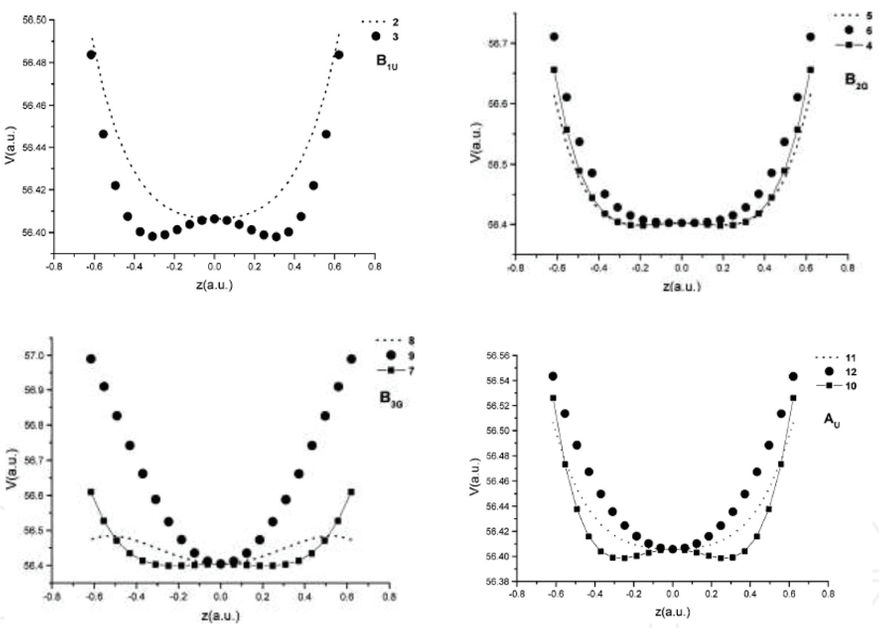

Figure 2. Dependence of the potential energy $V(z)$ (T = 415 K) upon the normal coordinates in the z(***c***) direction for D_{2h}^{16} symmetry $B_{1u}(2)$, $B_{1u}(3)$, $B_{2g}(4)$, $B_{2g}(5)$, $B_{2g}(6)$, $B_{3g}(7)$, $B_{3g}(8)$, $B_{3g}(9)$, $A_u(10)$, $A_u(11)$, and $A_u(12)$ normal modes.

where the coefficients $a = d = 0$ in the paraelectric phase. The displacements have been chosen in regard to the equilibrium positions of atoms. The curves $V(z)$ of symmetry $B_{1u}(3)$, $B_{2g}(4, 5)$, $B_{3g}(7)$, and $A_u(10)$ are correspondent to coefficients $b < 0$ and $c > 0$. These curves $V(z)$ have two side minima at distances of 0.3 a.u. from the equilibrium position. A potential barrier $\Delta V = b^2/4c$ separates the minima. Conversely, the curves $V(z)$ of symmetry $B_{1u}(2)$, $B_{2g}(6)$, $B_{3g}(8)$, $B_{3g}(9)$, $A_u(11)$, and A_u (12) have a single minima and the coefficients $b > 0$. The coefficient is $b \approx M\omega^2$,

where M represents the reduced mass of the normal mode atoms, and ω denotes the vibration frequency of the normal mode. The frequency of a normal mode with a double-well $V(z)$ is dependent on the height of the potential barrier ΔV. Temperature, electric field, pressure, and fluctuations of atoms in the x–y plane influence this potential barrier [15]. In all the three phases, $V(x)$ and $V(y)$ appear to be single-well with the coefficients $b > 0$ in Eq. (9). In the paraelectric phase, $a = d = 0$, whereas in the antiferro- and ferroelectric phases, $a \neq 0$ and $d \neq 0$. Single-well PE turns out to be weakly anharmonic and the frequencies of the $R(k)$ peak should only slightly depend on the temperature.

The experimental results of *IR* reflectivity $R(k)$ spectrum of SbSI crystals in the paraelectric (T = 415 K) and ferroelectric (T = 273 K) phases for $\boldsymbol{E}||\boldsymbol{c}$ are presented in **Figure 3**. The reflectivity measurements of SbSI crystals have been repeated by Dr. Markus Goeppert in Germany in Karlsruhe University using the Bruker Fourier spectrometer.

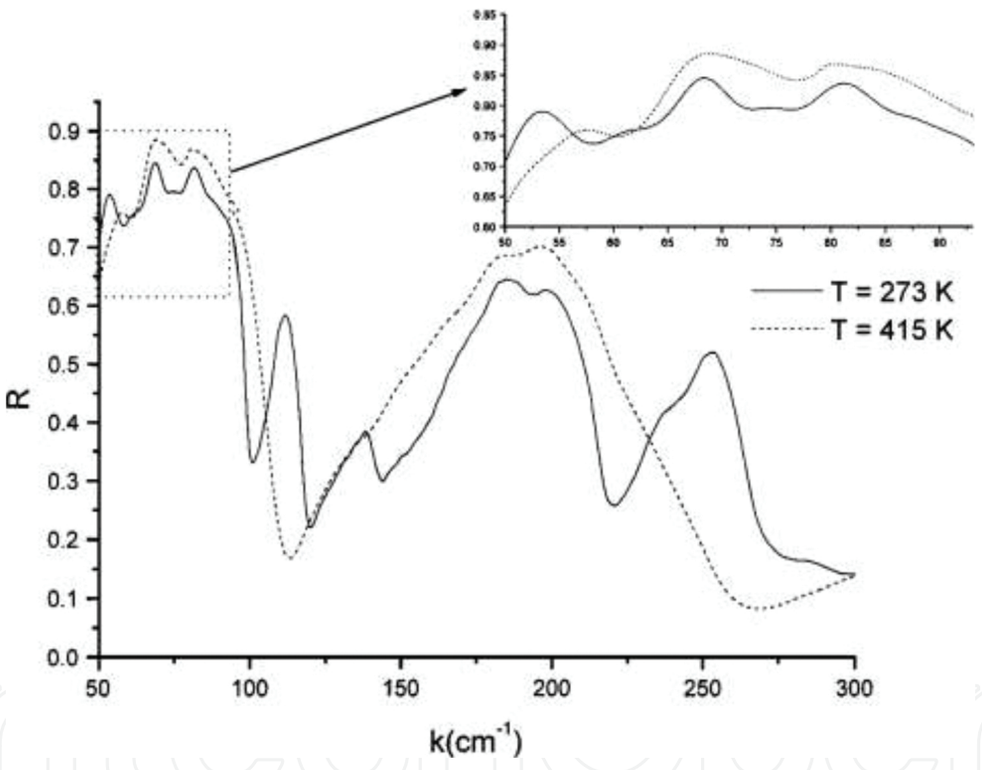

Figure 3. The reflectivity spectra of SbSI for $\boldsymbol{E}||\boldsymbol{c}$ in the paraelectric phase (T = 415 K) and in the ferroelectric phase (T = 273 K). Inset: the reflectivity spectra in range 50–95 cm^{-1}.

In the reflectivity spectrum for $\boldsymbol{E}||\boldsymbol{c}$ in the range of k = 10–100 cm^{-1}, the number of peaks $R(k)$ is equal for the paraelectric and ferroelectric phases. However, in the range of k = 100–200 cm^{-1}, the number of peaks $R(k)$ differs in both phases. Anharmonic modes with double-well $V(z)$ are highly sensitive to dislocations, impurities, and fluctuations of chains in the x–y plane.

Figure 2 demonstrates that modes $B_{1u}(3)$, $B_{2g}(4)$, $B_{2g}(5)$, and $B_{3g}(7)$ with a double-well $V(z)$ are strongly anharmonic, whereas modes $B_{1u}(2)$, $B_{2g}(6)$, $B_{3g}(8)$, and $B_{3g}(9)$ with a single-well $V(z)$ appear to be weakly anharmonic. The vibration frequencies of the former modes are lower

compared to the latter ones. Therefore, the $R(k)$ peaks are created by strongly anharmonic modes $B_{1u}(3) \rightarrow \boldsymbol{A_1}$, $B_{2g}(4) \rightarrow \boldsymbol{B_1}$, $B_{2g}(5) \rightarrow \boldsymbol{B_1}$, and $B_{3g}(7) \rightarrow \boldsymbol{B_2}$ in the range of k = 10–100 cm^{-1} of the *IR* spectrum. In the range of k = 100–400 cm^{-1}, the $R(k)$ peaks are created by weakly anharmonic modes. Following the optical selection rules, one $R(k)$ peak in the paraelectric phase is created by the mode $B_{1u}(2)$, while the peaks in the ferroelectric phase are created by modes $B_{1u}(2) \rightarrow \boldsymbol{A_1}$, $B_{2g}(6) \rightarrow \boldsymbol{B_1}$, $B_{3g}(8) \rightarrow \boldsymbol{B_2}$, and $B_{3g}(9) \rightarrow \boldsymbol{B_2}$. In the paraelectric phase, there are three silent modes of A_u symmetry: $A_u(10)$, $A_u(11)$, and $A_u(12)$ (**Table 3**). Two of them, $A_u(11)$ and $A_u(12)$, comply with the out-of-phase motion of the infrared-active modes. It is expected that the anharmonic mode $A_u(10)$ has a low frequency. This mode can be optically active and may cause a weak peak in the k <10 cm^{-1} *IR* range.

4. The piezoelectricity phenomena

4.1. Introduction

SbSI is a piezoelectric crystal that has a high-volume piezoelectric modulus $d_v = 10 \times 10^{-10}$ C/N and electromechanical coupling coefficient $k_3 = 0.87$ [25]. The relation among polarization P, piezoelectric modulus e, d, deformation $r = \Delta l/l$, and elastic compliance coefficient is as follows:

$$\Delta P = er, \Delta P \approx q\Delta z, \tag{10}$$

$$d = es. \tag{11}$$

where q is the atom's ionic charge, s is the elastic compliance coefficient, $\Delta z = z - z_0$, z_0 is the atomic equilibrium position, when crystal is not deformed ($r = 0$), and z is the atomic equilibrium position, when crystal is deformed ($r \neq 0$). It is handy to calculate the piezoelectric modulus d along $z(\boldsymbol{c})$-axis for needle-like crystal deforming it along the crystallographic axes $x(\boldsymbol{a})$, $y(\boldsymbol{b})$, and $z(\boldsymbol{c})$ when $r = \Delta a/a = \Delta b/b = \Delta c/c\ldots$ Having e it is possible to calculate d according to Eq. (11). The dependence of elastic compliance coefficients on temperature in SbSI crystal is shown in [26]. From work [27], piezoelectric module d_{33} along $z(\boldsymbol{c})$-axis and d_h (the so-called "hydrostatic piezoelectric modulus") were known. As d_h has been found to be of the same magnitude as d_{33}, it has been concluded that d_{31} is nearly equal to d_{32} and opposite in sign. Both quantities d_{32} and d_{31} are smaller than d_{33}. In [28] it is found that d_{31} is of the same order of magnitude as d_{33}. The d_{32} coefficient is of nearly the same value as d_{31} but opposite in sign. The high values of $d_h = d_{33} + d_{32} + d_{31}$ indicate that d_{31} and d_{32} are relatively small or of opposite in sign.

5. Potential energy of Sb atoms in anharmonic soft mode

In [29] we described the method for calculating the potential energy at point $\boldsymbol{r}$ of the unit cell. The potential energy at the point $\boldsymbol{r}$ is given in Eq. (7). The average value of the potential energy of Sb atoms of unit cell in the normal mode of SbSI crystal may be written as follows:

$$\bar{V}_p = \frac{V_p\left(\boldsymbol{R}_{\mathrm{Sb1}}\right) + V_p\left(\boldsymbol{R}_{\mathrm{Sb2}}\right) + V_p\left(\boldsymbol{R}_{\mathrm{Sb3}}\right) + V_p\left(\boldsymbol{R}_{\mathrm{Sb4}}\right)}{4}, \tag{12}$$

where $\boldsymbol{R}_{\mathrm{Sb1}} = \boldsymbol{R}_{0,\mathrm{Sb1}} + \boldsymbol{Q}_{\mathrm{Sb1}}$; $\boldsymbol{R}_{\mathrm{Sb2}} = \boldsymbol{R}_{0,\mathrm{Sb2}} + \boldsymbol{Q}_{\mathrm{Sb2}}$; $\boldsymbol{R}_{\mathrm{Sb3}} = \boldsymbol{R}_{0,\mathrm{Sb3}} + \boldsymbol{Q}_{\mathrm{Sb3}}$; and $\boldsymbol{R}_{\mathrm{Sb4}} = \boldsymbol{R}_{0,\mathrm{Sb4}} + \boldsymbol{Q}_{\mathrm{Sb4}}$.

Also, the coordinates of all *S* and *I* atoms changes according to the equations: $\boldsymbol{R}_\alpha = \boldsymbol{R}_{0,\alpha} + \boldsymbol{Q}_\alpha$, $\alpha = S_1; S_2; S_3; S_4; I_1; I_2; I_3; I_4$. For numerical evaluation of Eq. (12), we need to vary all $Q_\alpha = z_\alpha$ by small steps from $-Q_\alpha(\max)$ to $+Q_\alpha(\max)$. The atomic form factor is

$$f_\alpha(\mathrm{s}) = \sum_{nlm} nlm \left| \exp\left[\ i\left(\boldsymbol{r}\cdot\boldsymbol{s}\right)\right] \right| nlm, \tag{13}$$

where *nlm* is a set of quantum numbers for the atom α.

6. Antimony atoms' equilibrium positions

For theoretical investigations, we used the most sensitive to temperature and deformations soft mode's $\bar{V}_p(z)$ dependence on normal coordinates [29]. It is handy to expand $\bar{V}_p(z)$ using polynomial:

$$\bar{V}_p(z) = V_0 + a^* z + b^* z^2 + d^* z^3 + c^* z^4, \tag{14}$$

where a^*, b^*, d^*, and c^* are polynomial expansion coefficients.

The $\bar{V}_p(z)$ dependence on normal coordinates along $z(\boldsymbol{c})$-axis in paraelectric phase (PEF) at $T = 300$ K is shown in **Figure 4** while deforming along $x(\boldsymbol{a})$, $y(\boldsymbol{b})$, and $z(\boldsymbol{c})$ axes. The $\bar{V}_p(z)$ in PEF has a shape of double-well ($b^* < 0$, $c^* > 0$). The barrier height when crystal is not deformed is $\Delta U_C \approx kT_C$, where k is the Boltzmann constant. As seen from **Figure 4**, in paraelectric phase Δz are equal to zero, because $\bar{V}_p(z)$ of Sb atomic soft mode is symmetrical and double-well. In paraelectric phase, Sb atoms vibrate between two minima of double-well potential $\bar{V}_p(z)$, provided deformation $r \neq 0$ and $r = 0$.

http://dx.doi.org/10.5772/64223

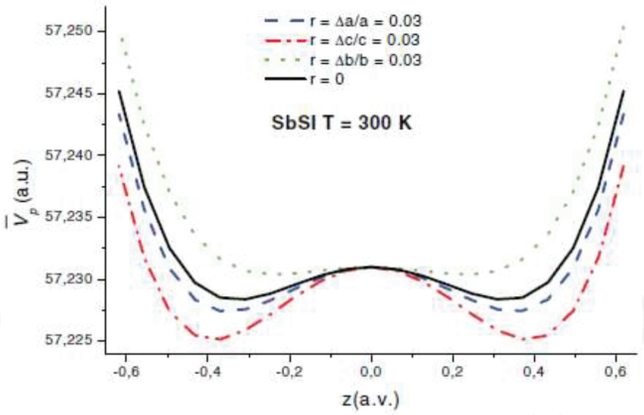

Figure 4. The SbSI mean potential energy dependence on soft mode normal coordinates at the Sb atoms sites in paraelectric phase (T = 300 K), when deformation r = 0.03 along $x(\boldsymbol{a})$, $y(\boldsymbol{b})$, and $z(\boldsymbol{c})$ axes and r = 0. Δz = 1 a.u. = 0.53 Å.

Due to the decrease in the temperature in ferroelectric phase, double-well $\overline{V}_p(z)$ gradually changes its form (see **Figure 2**) from double-well to single-well ($a^* \neq 0$, $b^* < 0$, $d^* \neq 0$, $c^* > 0$).

We calculated SbSI crystal's Sb atom potential energy's dependence on soft mode's normal coordinates in FEF at T = 289 K, when crystal is deformed along $x(\boldsymbol{a})$, $y(\boldsymbol{b})$, and $z(\boldsymbol{c})$ axes, and when crystal is not deformed (r = 0; **Figure 5**). z_0 is the equilibrium position of Sb atom when $r = 0$ and z is the Sb atom's equilibrium position when $r \neq 0$. Calculated temperature dependence of z, $\Delta z = z - z_0$, and $\overline{V}_p(z)$ scanning coefficients a^*, b^*, d^*, and c^* are shown in **Tables 4** and **5**. Temperature dependence of equilibrium position z_0 of Sb atoms in ferroelectric phase (when r = 0) is calculated using Eq. (8):

$$z_0 = 0.24988 + 0.00221\,T - 3.13691E-5\,T^2 + 1.42721E-7\,T^3 - 2.37137E-10\,T^4\,(\text{Å}),$$

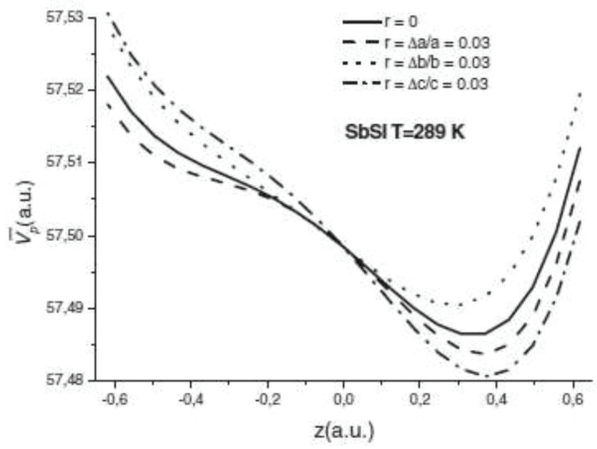

Figure 5. The SbSI mean potential energy dependence on soft mode normal coordinates at the Sb atoms sites in ferroelectric phase (T = 289 K), when deformation r = 0.03 along $x(\boldsymbol{a})$, $y(\boldsymbol{b})$, and $z(\boldsymbol{c})$ axis and r = 0. Δz = 1 a.u. = 0.53 Å.

T, K	*a**	*b**	*c**	*d**	*r*
300	0	−0.058422	0.237293	0	0
	0	−0.078223	0.260437	0	$\Delta c/c$
	0	−0.021201	0.188036	0	$\Delta b/b$
	0	−0.068322	0.248865	0	$\Delta a/a$
292	−0.015845	−0.049218	0.221618	0.034324	0
	−0.016505	−0.069437	0.245634	0.035488	$\Delta a/a$
	−0.014301	0.013858	0.179530	0.030567	$\Delta b/b$
	−0.030185	0.051400	0.226095	0.031457	$\Delta c/c$
289	−0.044289	−0.030932	0.207956	0.094969	0
	−0.046523	−0.049664	0.228457	0.099234	$\Delta a/a$
	−0.039959	0.004717	0.164141	0.084533	$\Delta b/b$
	−0.05896	−0.033813	0.210681	0.093388	$\Delta c/c$

Table 4. Scanning coefficients a^*, b^*, c^*, and d^* at different temperatures in SbSI crystal when crystal is not deformed ($r = 0$) and deformed along $x(\boldsymbol{a})$, $y(\boldsymbol{b})$, and $z(\boldsymbol{c})$ axes, when $r = \Delta a/a = \Delta b/b = \Delta c/c = 0.03$.

T, K	Δz_{31}, a.u.	Δz_{32}, a.u.	Δz_{33}, a.u.
300	0	0	0
292	0.0759	−0.068310	0.097
289	0.0487	−0.04383	0.0694
274	0.0329	−0.02961	0.0384
250	0.0228	−0.02052	0.0284
225	0.0173	−0.01557	0.0219
195	0.0142	−0.01278	0.019
170	0.0141	−0.01269	0.0158
150	0.0124	−0.01116	0.0152
130	0.0107	−0.00963	0.0137

Table 5. Temperature dependence of Sb atom's equilibrium positions displacements' Δz_{31}, Δz_{32}, and Δz_{33} along $x(\boldsymbol{a})$, $y(\boldsymbol{b})$, and $z(\boldsymbol{c})$ axes when deformation is $r = \Delta a/a = \Delta b/b = \Delta c/c = 0.03$, respectively. $\Delta z = 1$ a.u. = 0.53 Å.

where $T < T_C$ is the temperature of the SbSI crystal in ferroelectric phase.

Since $e = \frac{\Delta P}{r}$ and r = const., then $e \approx \Delta P \approx \Delta z$. Consequently, using the data from **Table 5** we present Δz dependence on temperature, when crystal is being deformed equally along three axes: $r = \Delta a/a = \Delta b/b = \Delta c/c$ (**Figure 6**).

http://dx.doi.org/10.5772/64223

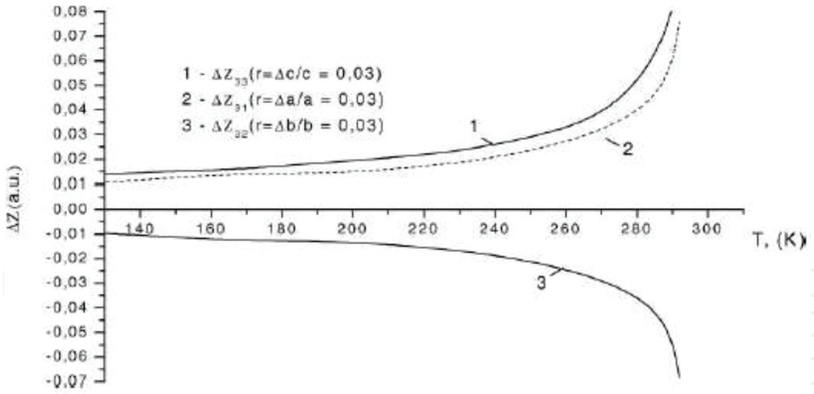

Figure 6. Temperature dependence of Sb atom's equilibrium position's displacements' Δz_{31}, Δz_{32}, and Δz_{33} along $x(\boldsymbol{a})$, $y(\boldsymbol{b})$, and $z(\boldsymbol{c})$ axes when deformation of SbSI crystal is $r = \Delta a/a = \Delta b/b = \Delta c/c = 0.03$, respectively, $\Delta z = 1$ a.u.

Figures 4 and **6** show that close to T_C potential energy of Sb atoms $\overline{V}_p(z)$ and Sb atom's equilibrium position's displacements Δz_{31}, Δz_{32}, and Δz_{33} are very sensitive to the temperature changes and deformation of SbSI crystal. In temperature range $T < 250$ K, the sensitivity of $\overline{V}_p(z)$ and $\Delta z_{31} \sim e_{31}$, $\Delta z_{32} \sim e_{32}$, $\Delta z_{33} \sim e_{33}$ to their temperature changes and deformation directly decreased.

In **Figure 7**, we compared theoretical results of Sb atoms $\Delta z_{33} \sim e_{33}$ from **Table 5** with experimental piezoelectric modulus $e_{33} = d_{33}/s$ from [2, 11] dependence on temperature when crystal is deformed in direction of $z(\boldsymbol{c})$-axis.

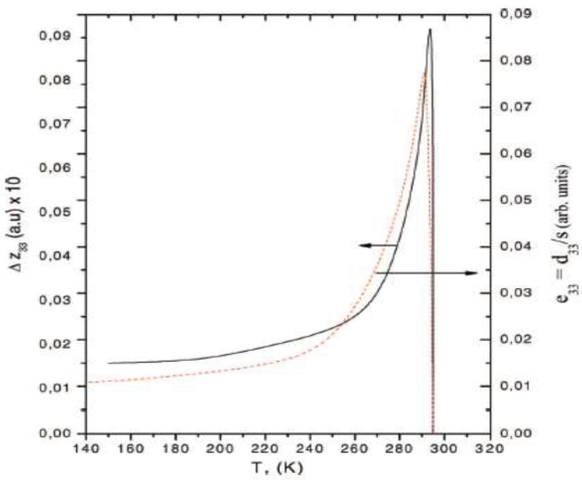

Figure 7. Temperature dependence of Sb atom's equilibrium position's displacement Δz_{33} along $z(\boldsymbol{c})$-axis and experimental [2, 11] piezoelectric modulus $e_{33} = d_{33}/s$. $\Delta z = 1$ a.u.

As seen from **Figure 7**, the temperature dependences of Sb atom's equilibrium position's displacements $\Delta z_{33} \sim e_{33}$ coincide well with experimental piezoelectric modulus $e_{33} = d_{33}/s$ when crystal is deformed in direction of $z(\boldsymbol{c})$-axis because Δz_{33} is created by anharmonic Sb atom's potential energy $\overline{V}_p(z)$.

Existence of the piezoelectric effect experimentally detected up to a temperature several degrees above the T_C (**Figure 4**). The effect above T_C (**Figure 7**) may be attributed to the compositional inhomogeneity or the existence of the internal mechanical stresses.

7. Electron-phonon interaction and Jahn-Teller effect (JTE)

7.1. Introduction

Examining the state of instability, the authors [30] have determined that in this respect the normal coordinate of the vibrational mode is $K = K_0 - K_v < 0$, where $K_0 = 1/2\ \mathrm{M}\frac{2}{0}$ represents the bare force constant, while K_v stands for a vibrational coupling term, which is dependent on the vibrational coupling constant F and the energy gap ΔE. C_{2h}^2 operations are $S_1 = E/(0,0,0)$, $S_2 = C_2(z)/(0,0,1/2)$, $S_3 = I/(0,0,0)$, and $S_4 = \sigma_z/(0,0,1/2)$ for the PEP space group, whereas only S_1 and S_2 are for the FEP space group C_{2h}^2. The movement of atoms within the chain is marked by energy states of independent normal vibrations, associated with vibrational symmetry coordinates that are composed of the projections of atomic displacements $K_i = X_i, Y_i, Z_i$ on the axes of local coordinate systems [31, 32]:

$$\chi_j^{(\alpha)} = N^{(\alpha)} \sum_i c_{ji} K_i \tag{15}$$

$\Gamma_\alpha(C_2^2)$	$\Gamma_\alpha(C_{2h}^2)$	S_1	S_2	S_3	S_4
A	A_g	+1	+1	+1	+1
B	B_g	+1	−1	+1	−1
A	A_u	+1	+1	−1	−1
B	B_u	+1	−1	−1	+1

Table 6. Characters of irreducible representations of symmetry space group C_2^2, and C_{2h}^2.

The coefficients c_{ji} are developed from the properties of irreducible representations Γ_a obtained when coordinates $\chi^{(\alpha)}$ with symmetry operations S_i are transformed (see **Table 6** for the characters of the representations). Symmetry coordinates that are composed of projections Z_i of atomic displacements usually have symmetry A_u and B_g, whereas the coordinates that are composed of projections X_i and Y_i possess symmetry A_g and B_u. Consequently, by solving the system of vibrational equations, normal coordinates $Q_i^{(\alpha)}$ are obtained, in which X_i and Y_i are interlinked and Z_i participates separately. Thus, the normal vibrations in the SbSI chain along the z-axis can be characterized by A_u and B_g symmetry coordinates, whereas the vibrations in the direction of x- and y-axes are related to B_u and A_g symmetry coordinates. The modes

$X_7(B_u)$ and $X_{13}(B_u)$ comply with acoustic vibrations, whereas the remaining ones correspond to the optical vibrations of the SbSI chain (**Table 7**).

$\Gamma_\alpha(C_2^2)$	$\Gamma_\alpha(C_{2h}^2)$	$N^{(\alpha)}$	Sb3	Sb4	S3	S4	I1	I2	K_i
A	A_u	$\frac{1}{\sqrt{6}}$	+1	+1	+1	+1	+1	+1	z(1)
A	A_u	$\frac{1}{\sqrt{12}}$	+1	+1	+1	+1	−2	−2	z(2)
A	A_u	$\frac{1}{\sqrt{2}}$	+1	+1	−1	−1	0	0	z(3)
B	B_g	$\frac{1}{\sqrt{6}}$	+1	−1	+1	−1	+1	−1	z(4)
B	B_g	$\frac{1}{\sqrt{12}}$	+1	−1	+1	−1	−2	+2	z(5)
B	B_g	$\frac{1}{\sqrt{2}}$	+1	−1	−1	+1	0	0	z(6)
B	B_u	$\frac{1}{\sqrt{6}}$	+1	+1	+1	+1	+1	+1	x,y(7, 13)
B	B_u	$\frac{1}{\sqrt{12}}$	+1	+1	+1	+1	−2	−2	x,y(8, 14)
B	B_u	$\frac{1}{\sqrt{2}}$	+1	+1	−1	−1	0	0	x,y(9, 15)
A	A_g	$\frac{1}{\sqrt{6}}$	+1	−1	+1	−1	+1	−1	x,y(10,16)
A	A_g	$\frac{1}{\sqrt{12}}$	+1	−1	+1	−1	−2	+2	x,y(11, 17)
A	A_g	$\frac{1}{\sqrt{2}}$	+1	−1	−1	+1	0	0	x,y(12, 18)

Table 7. Vibrational symmetry coordinates in the simplified unit cell of the SbSI chain.

8. Electron-phonon interaction in one atomic chain

Figure 2 provides the dependence of one-electron energies in the valence band of a long SbSI chain on the number of atoms N, which is calculated by the unrestricted Hartree-Fock method (UHF) [33] in the basis set of H_w functions using the pseudopotential. As it is seen from **Figure 2**, the highest energy levels in the valence band degenerate when N turns to 40 or more. As it is shown in **Figure 3**, the highest A_u and A_g one-electron energy levels are degenerated in the PEP close to the band gap. The lowest levels of the conduction band are set apart from the highest levels of the valence band by a band gap of E_g = 5.712 eV.

Table 8 has been composed with reference to **Table 7**, where symmetry types of one-electron levels are presented. In **Table 8**, the energies of the degenerate A_u and B_g symmetry electronic levels in the valence band are highlighted by boldface, where the energies of level 177 B_g and level 178 A_u are −0.3344H, and the energies of level 179 A_u and level 180 B_g are −0.3257H (assuming that 1 H = 27.21 eV).

Valence band		**Conduction band**	
Symmetry	Energy (H)	Symmetry	Energy (H)
176 B_g	−0.3363	181 A_u	−0.0926
177 B_g	**−0.3344**	182 B_g	−0.0925
178 A_u	**−0.3344**	183 A_u	−0.0847
179 A_u	**−0.3257**	184 B_g	−0.0838
180 B_g	**−0.3257**	185 A_u	−0.0821

Note: The degenerate electronic states in the valence band are denoted by boldface.

Table 8. One-electron energies in the conduction band bottom and valence and top for an SbSI chain containing $N = 60$ atoms.

In the phase transition, i.e., when equilibrium positions of the Sb and S atoms alter along the z(*c*)-axis, the degeneracy is removed, and the band gap E_g is narrowed. The decrease of the interatomic force factor R determines the decrease of E_g (**Figure 8a**). However, the ionic charges q has no influence on the decrease of E_g, as they remain almost constant throughout the phase transition (**Figure 8b**).

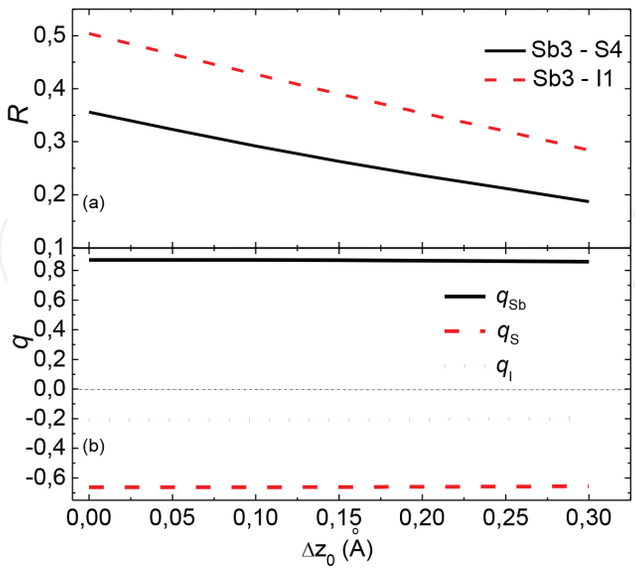

Figure 8. The variation of the interatomic bond strengths R and atomic charges q in the SbSI chain containing 60 atoms during the phase transition. Here z_0 denotes the displacement of Sb atoms in the direction of z-axis.

The normal vibrational mode of symmetry A_u (further for clarity denoted here as $_u$) interacts with the electronic states of symmetry A_u and B_g if $A_u \times B_g = {}_u$. The electron-phonon interaction involving the highest degenerate A_u and B_g symmetry levels of the valence band is called the Jahn-Teller effect. The pseudo-Jahn-Teller effect (PJTE) occurs when the normal $_u$ mode interacts with the A_u electronic state at the top of the valence band and with the B_g electronic state at the bottom of the conduction band, as well as with the band gap of E_g between them. Because of the PJTE, the dependence of the harmonic term $\varepsilon_{f.e}$ on normal coordinates Q is split into two terms:

$$\varepsilon_{f.e}(Q) = \frac{1}{2}\left(K_0 - \frac{2F^2}{E_g}\right)Q^2 \tag{16}$$

where K_0 represents nonvibronic part of the force constant (the bare force constant), K_V stands for the vibronic coupling term. $K = K_0 - (2F^2/E_g) = K_0 - K_v$ denotes the force constant considering the PJTE. F which is found from the following equation represents the vibronic coupling constant:

$$F^2 = \frac{\Delta E E_g}{2Q_0^2}. \tag{17}$$

Here $Q_0 = z_0$ is the atomic displacement, and ΔE is the variation of the band gap during the phase transition. From **Figure 9** and Eq. (17), it follows that for $z_0 = 0.2$ Å, $\Delta E = 2.23$ eV, and $E_g = 5.7$ eV, we would get $F \approx 13$ eV/Å. From the experimental results of Ref. [34], we derived $F \approx 4$ eV/Å. Therefore, the magnitude of the term $2F^2 = E_g$ may attain as much as 2H/Å.

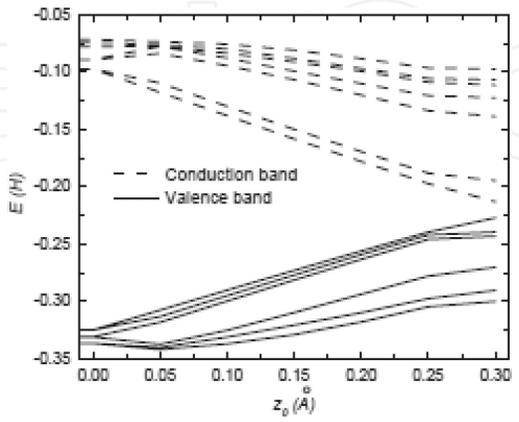

Figure 9. The variation of the one-electron energy spectrum of the SbSI chain containing 60 atoms during the phase transition. Here z_0 denotes the displacement of Sb atoms in the direction of z-axis.

In the case of the normal mode $_u$, the PJTE and JTE vibronic mixing leads to the force constant

$$K = K_0 - \left(\frac{2F^2}{E_g} + G \right) = K_0 - K_V^*,$$

State	AFEP (T = 300 K)		FEP (T = 215 K)			
			Left edge of cluster		Right edge of cluster	
	E_{max} (eV)	E_{min} (eV)	E_{max} (eV)	E_{min} (eV)	E_{max} (eV)	E_{min} (eV)
I 3 s	1030.40	1027.72	1028.69	1025.72	1032.09	1029.87
Sb 3 s	917.51	916.66	918.17	915.10	919.59	918.17
I 3p	891.44	888.70	889.73	886.70	893.12	890.83
Sb 3p	787.89	786.98	785.73	785.42	789.97	788.52
I 3d	658.75	655.99	657.04	653.99	660.44	658.12
Sb 3d	567.67	565.74	565.41	565.19	569.13	568.24
S 2 s	244.78	243.29	242.96	241.21	246.45	245.35
I 4 s	198.47	195.77	196.78	193.76	200.16	197.93
S 2p	181.47	179.59	179.66	177.81	183.13	181.94
Sb 4 s	170.09	169.27	167.95	167.71	172.13	170.80
I 4p	147.59	144.70	145.92	142.72	149.26	146.55
Sb 4p	123.97	123.04	121.86	121.48	126.01	124.55
I 4d	67.13	64.11	65.45	62.14	68.82	66.23
Sb 4d	51.35	50.35	49.25	48.80	53.38	51.87

Table 9. The energies of CL of Sb, S, and I atoms calculated by UHF method at the edge of SbSI cluster.

where G is a quadratic vibronic constant from JTE, and K_V^* is the vibronic coupling term of PJTE and JTE. The phase transition occurs when the low-frequency mode is unstable, i.e., when $K < 0$, see **Table 9**. The symmetry coordinates of this mode are Sb(+1), S(+1), and I(−2). In pursuance of finding K, the total energy E_T of the $_u$ vibrational mode has to compute. Separate energy contributions constitute the total energy E_T:

$$E_T = E_K + E_{ee} + E_{ne} + E_{nn}, \tag{18}$$

where the kinetic energy of electrons is

http://dx.doi.org/10.5772/64223

$$E_{\mathrm{K}} = \sum_{i=1}^{n} \frac{\overrightarrow{P}_i^{\,2}}{2m_c}, \tag{19}$$

the interelectron interaction energy is

$$E_{\mathrm{ee}} = \frac{1}{2}\sum_{i,j\neq i}^{n} \frac{e^2}{\left|\vec{r}_i - \vec{r}_j\right|}, \tag{20}$$

the electron-nuclear interaction energy is

$$E_{\mathrm{ne}} = -\sum_{i,A=1}^{n,N} \frac{e^2 Z_A}{\left|\vec{R}_A - \vec{r}_i\right|}, \tag{21}$$

and the internuclear interaction energy is

$$E_{\mathrm{nn}} = \frac{1}{2}\sum_{A,B\neq A}^{N} \frac{e^2 Z_A Z_B}{\left|\vec{R}_A - \vec{R}_B\right|}. \tag{22}$$

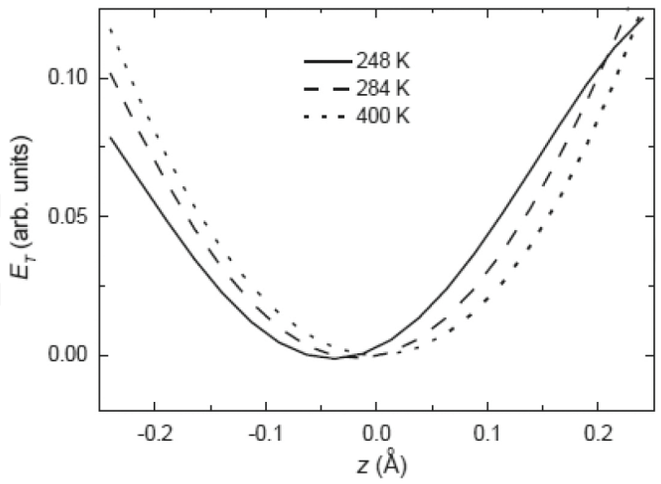

Figure 10. The dependence of the total energy E_{T} of the $_u$ mode upon normal coordinates (relative displacements Z_α of atoms (α = Sb, S, I) from equilibrium position), where z denotes the displacement of Sb atoms in the $\widetilde{\mathrm{A}}_{\mathrm{u}}$ mode from their equilibrium position. The temperatures of the chain are 400 K in PEP and 284 and 248 K in FEP. In all cases E_{T0} = 0.

The aforesaid energies are dependent on nuclear and electronic coordinates $\vec{R}, \vec{r}_i$. Their evaluation has been conducted with the unrestricted Hartree-Fock method using the computer program GAMESS described in [33]. In pursuance of finding K, the dependence of the total energy E_T of the $_u$ mode has been computed on the displacements z_α of atoms (α = Sb, S, I) from their equilibrium positions (**Figure 10**). **Figure 10** demonstrates that z measures the displacements of Sb atoms in the $_u$ mode from their equilibrium positions $z_{0\alpha}$. Vibrational displacements z_α of atoms (α = Sb, S, I) from their equilibrium positions $z_{0\alpha}$ are identified employing the equation

$$z_\alpha = z_\alpha \pm u_\alpha \frac{1}{\sqrt{m_\alpha}} \cdot \frac{i}{20}, \tag{23}$$

where i = 0–19, $u_\alpha\, m_\alpha^{-1/2}$ is the vibrational amplitude of atoms (u_α is the normal coordinates of the $_u$ vibrational mode). Normal coordinates of the $_u$ vibrational mode are found by diagonalization of the dynamical matrix [23].
By expressing $E_T = f(z)$ as a fourth-order polynomial

$$E_T = E_{T0} + K(z)^2 + c(z)^4. \tag{24}$$

For the $_u$ mode in PEP (300 K), K = 2.05 H/Å^2 and c = 2.3 H/Å^4. Since the obtained K value is positive, it is supposed that the electron-phonon interaction will only decrease K. The interaction itself will not induce a phase transition because under the influence of the electron-phonon interaction the $_u$ mode becomes only slightly anharmonic. However, due to phonon-phonon interaction in the SbSI chain, the $_u$ mode is strongly anharmonic, as its $K < 0$ and $c > 0$ [14]. Simultaneous action of electron-phonon and phonon-phonon interactions increase even more the anharmonicity of the $_u$ mode as compared to its anharmonicity determined by the phonon-phonon interaction alone. Therefore, the phase transition in the SbSI crystals is due to both electron-phonon and phonon-phonon interactions.

9. Physical parameters in the phase transition region

The vibration frequencies of the normal mode A_u are temperature dependent [10]. Therefore, the influence of the electron-phonon interaction and variation of unit cell parameters in the phase transition region on temperature dependence of frequency should be assessed properly.

http://dx.doi.org/10.5772/64223

By putting vibrational displacements z_α of atoms (α = Sb, S, I) from their equilibrium positions equal to $z_\alpha = 0$, Eq. (24) is transformed into

$$E_{T0} = E_{K0} + E_{ee0} + E_{ne0} + E_{nn0}. \tag{25}$$

It follows from Eqs. (18) and (22) that separate terms in Eq. (25) are functions of atomic coordinates $\vec{R}$ and distances between atoms $(\vec{R}_A - \vec{R}_B)$ During the phase transition, due to variation of the volume of the simplified unit cell $V_0 = (a/2)bc$ [30]. Just this causes anomalies in the temperature dependences of E_{T0} and its separate components in the phase transition region **Figures 9** and **11**. **Figure 11** demonstrates temperature dependences of E_{T0} and of the unit cell volume V_0.

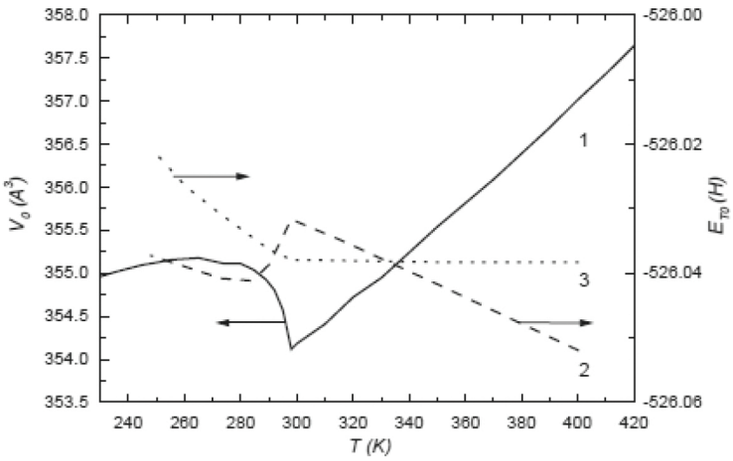

Figure 11. Temperature dependences of the unit cell volume $V_0 = 2$ V (where V is the volume of the simplified unit cell) (1) and of the total energy E_{T0} (2) in the phase transition region. For curve 2, V_0 is assumed to depend upon temperature, and for curve 3 it is taken as constant: $V_0 = 354.25$ Å^3.

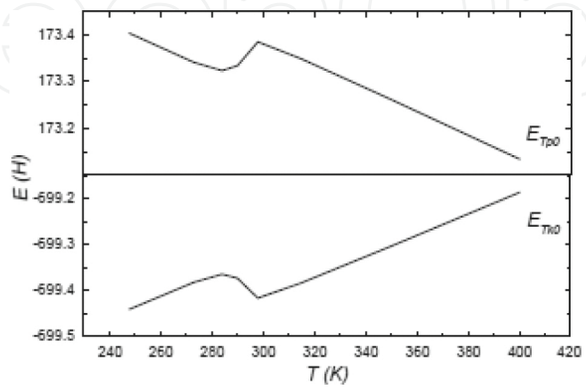

Figure 12. Temperature dependences of the total kinetic E_{TK0} and potential energy E_{TP0} in the phase transition region.

In PEP (or in the antiferroelectric phase, according to Ref. [14]), the anomalies of E_{T0} and V correlate in the temperature range of 295–400 K. It means that E_{T0} decreases due to the growth of V_0, and vice versa. **Figures 12** and **13** show that the temperature dependence of E_{T0} is mainly determined by the components $E_{TP0} = E_{ee0} + E_{ne0} + E_{nn0}$.

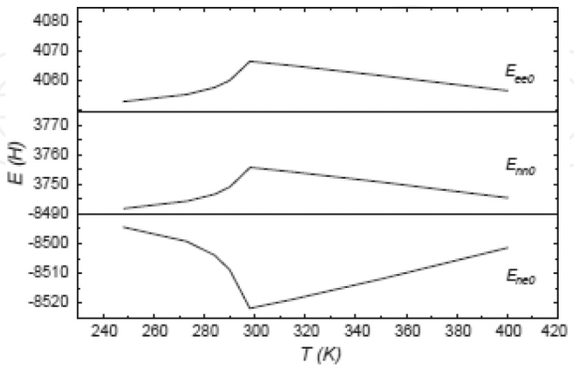

Figure 13. Temperature dependences of the total potential energy E_{TP0} components E_{ee0}, E_{ne0}, and E_{nn0} in the phase transition region.

In the FEP in the temperature range 280–295 K, a sharp increase of the unit cell volume V_0 leads to a decrease of E_{T0}, curves 1 and 2 in **Figure 11**. However, in FEP at the temperatures of 220–280 K, E_{T0} grows if the temperature is decreased, while the unit cell volume V_0 changes only slightly. Curve 3 in **Figure 11** shows the calculated temperature dependence of E_{T0} provided that V_0 = constant. In this temperature range, when V_0 = constant, the growth of E_{T0} is caused by the variable shift of the equilibrium positions of Sb and S atoms. Thus, curve 2 in **Figure 11** demonstrating the growth of E_{T0} can also be considered as caused solely by the variation of Sb and S equilibrium positions.

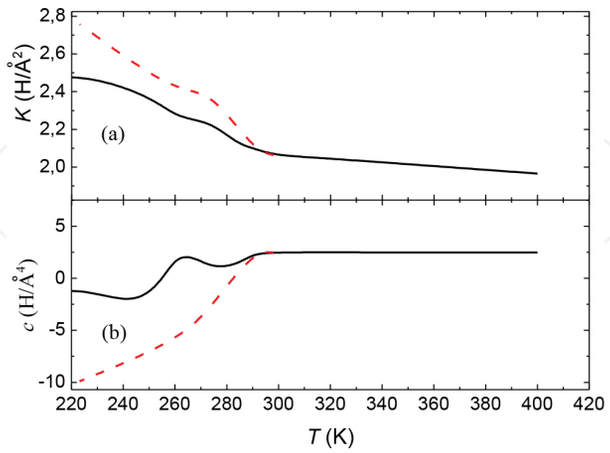

Figure 14. Temperature dependences of the harmonic constant $K = (K_0 - K_V^*)$ Å and of the anharmonicity factor c (B) for the $\widetilde{A}_u$ normal mode in the phase transition region. Dashed lines show the temperature dependences of K and c assuming that $V_0 = 354.25$ Å^3.

The three temperature intervals, i.e., 295–400 K in PEP, 280–295 K in FEP, and 220–280 K in FEP, clearly reveal the anomalies in the temperature dependences of the coefficients K and c of the polynomial (10) (**Figures 14a** and **b**). The temperature dependences of K and c are determined by the variation of the unit cell volume V_0 in the PEP interval at 295–400 K, whereas the behavior of K and c is determined by V_0 and the variable shift of the equilibrium positions of Sb and S atoms in the FEP interval at 280–295 K.

Pursuing to separate the influence of the volume V_0 and of the shift of Sb and S equilibrium positions on the anomalies of K and c, the calculated temperature dependences of K and c at a constant V_0 are demonstrated in **Figures 14(a)** and **(b)** (dashed lines). In this temperature range, K and c rapidly change due to the variation of the equilibrium position of Sb and S atoms if V_0 = constant. Consequently, the rapid change of K and c marked by the solid lines in **Figures 14(a)** and **(b)** is also caused merely by the shift of Sb and S atoms. The rapid variation of K in this temperature range occurs due to the decrease of K_V^* that is determined by thevariation

of degeneracy (see **Figure 9**). Since $K = m_\tau^2$, where m_τ is the reduced mass of the $_u$ mode and ω is the frequency of this mode, then the dependence of K upon temperature (**Figure 14a**) is similar in its shape to the temperature dependence of the soft mode ^2_s [14]. Therefore, the

temperature dependence of the soft mode $_u$ frequency ^2_s is essentially affected by the variation of the unit cell volume V and of the polynomial coefficient K in the phase transition region: the total temperature dependence of ^2_s can be obtained provided the anharmonicity caused by phonon-phonon interaction is considered.

10. The electronic structure of SbSI cluster at the phase transition region

10.1. Introduction

As it is known [25, 34, 35], a ferroelectric phase transition of the first kind occurs in SbSI, though it is close to the phase transition of the second kind. What is more, it has been theoretically proved in Ref. [36] that the phase transition in SbSI takes an intermediate position between order-disorder and displacement types. In general, it is known that ferroelectric phase is at $T < T_C = 295$ K, antiferroelectric phase exists at $T_C < T < 410$ K, and paraelectric phase at $T > 410$ K.

Lukaszewicz et al. [17] determined the crystal structure of SbSI in the temperature region at 170–465 K. They found that there are three phases in the phase diagram of SbSI: ferroelectric phase (FEP) III (space group $Pna2_1$) below T_{C1} = 295 K, antiferroelectric phase (AFEP) II ($P2_12_12_1$) in the temperature region (T_{C2} = 295–410 K), and high temperature paraelectric phase (PEP) I above 410 K. AFEP is characterized by the double polar chains $[(SbSI)_1]_2$, which are ordered antiferroelectrically: these cause a disorder in the crystal lattice. Experimental investigation of X-ray absorption, fluorescence, and electron emission [37, 38] adjusts the energy band structure of SbSxSe1−xI (x = 0.25; 0.5; 1), SbSBr. Its explanation necessitates for a more precise calculation of the contribution of separate atoms to the total density of states. The

authors [39] had measured X-ray photoelectron emission spectra (XPS) of the SbSI crystals of valence bands (VB) and core levels (CL). XPS results showed the splitting of the CL. However, they have not explained theoretically the XPS spectra of the VB.

11. *Ab initio* method description

The UHF method in the MOLCAO approximation serves as the basis of the method of calculation. The molecular orbital (MO) (φ_i) can be expanded in the atomic orbital (AO) $\chi_\mu(\mathbf{r})$ basis set

$$\varphi_i(\boldsymbol{r}) = \sum_{\mu}^{Ci\mu} \chi_\mu(\boldsymbol{r}). \tag{26}$$

Here μ denotes the number of AO. Matrix C is obtained by solving the Hartree-Fock matrix equation

$$FC = ESC. \tag{27}$$

The roots of this secular equation lie in the molecular energies E_i of electrons, where F stands for the Fockian matrix and S for the matrix of overlap integrals:

$$S_{\mu\nu} = \int \chi_\mu \chi_\nu d\boldsymbol{r}. \tag{28}$$

The coefficients $C_{i\mu}$ allowed us to find the density matrix of the electron distribution:

$$P_{\mu\nu} = 2\sum_{i=1}^{N/2} C_{i\mu} C_{i\nu}, \tag{29}$$

where N is the number of electrons, and the sum is over all occupied MO. We can find the bond order between the A and B atoms,

$$P_{AB} = \sum_{\mu \in A} \sum_{\nu \in B} P_{\mu\nu} \tag{30}$$

http://dx.doi.org/10.5772/64223

and the charge of atoms,

$$\rho_A = Z_A - \sum_{\mu \in A} P_{\mu\mu} \tag{31}$$

The calculations were performed by the GAMESS program [33]. Atomic coordinates have been used from the work of Lukaszewicz et al. [17].

12. Investigation of SbSI crystal valence band

The paraelectric structure ($T > T_{C2} = 410$ K) of SbSI is made of atom chains that belong to the paraelectric space group Pnam, which form square-pyramidal S_3I_2 groups with the Sb ion at the center of the pyramid base. All atoms lie on mirror planes normal to the ***c***-axis (**Figure 15**).

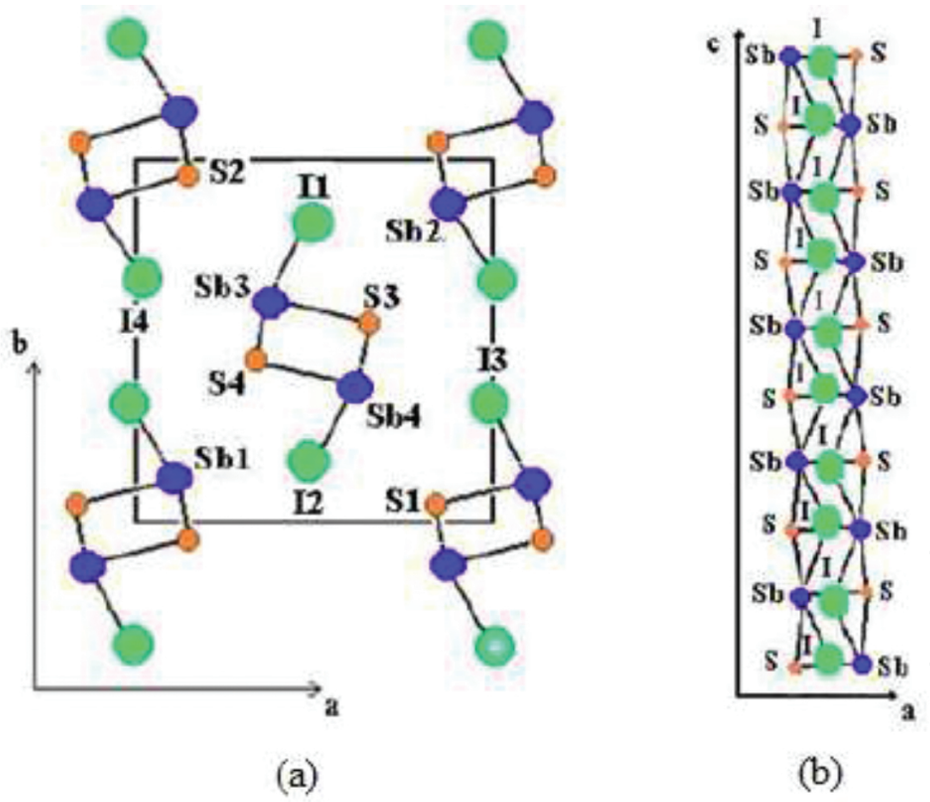

Figure 15. Crystal structure of SbSI projected on the **a**–**b** plane (a), and one double chain of molecular cluster in projection on the **a**–**c** plane (b).

On passage into the AFEP ($T_{C2} > T > T_{C1} = 295$ K) and FEP ($T < T_{C1}$), the position parameters normal to the ***c***-axis are substantially unchanged. In AFEP ($T = 300$ K) the displacements of equilibrium position occur for all Sb3 atoms along the ***c***-axis $z_0 = 0$, 02 Å and for all Sb4 atoms

(z_0 = −0, 02 Å) [37]. In FEP ($T < T_{C1}$) all Sb and S atoms move along the ***c***-axis toward these I sites, which leads to the removal of the mirror plane symmetry. In FEP (T = 215 K), the displacements of equilibrium position occur for all Sb atoms along the ***c***-axis z_0 = 0, 2 Å.

The molecular cluster model of one SbSI crystal chain was used to perform the theoretical *ab initio* calculation of energy levels (**Figure 15**). As seen from **Figure 16**, energy levels only slightly change with the increase of the cluster. **Figure 17** shows that the energy of some levels increases and of others decreases.

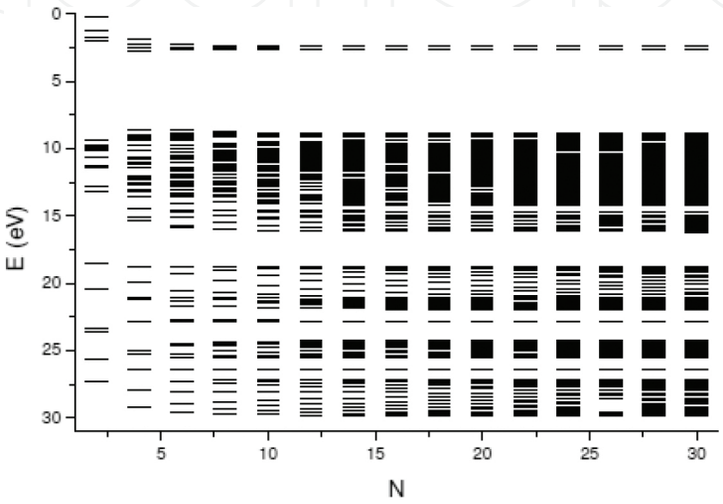

Figure 16. Dependence of energy levels of VB on the number N of SbSI molecules in a molecular cluster in AFEP (300 K).

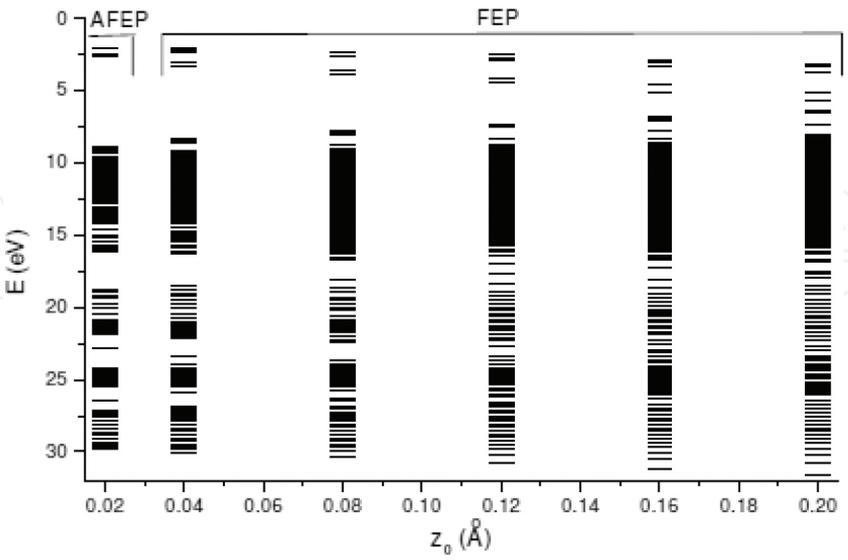

Figure 17. Dependence of energy levels of VB on equilibrium positions z_0 of Sb atoms in SbSI molecular cluster. The displacements of equilibrium position z_0 of Sb atoms: for all Sb3 atoms in AFEP (300 K), z_0 = 0, 02 Å, and for all Sb4 atoms z_0 = −0, 02 Å; z_0 = 0, 2 Å, for all Sb3 and Sb4 atoms in FEP (215 K).

We have calculated the bond orders between the atoms Sb3-S4, Sb4-S3, Sb3-I1, and Sb4-I2 along a cluster in AFEP and FEP (**Figures 18** and **19**). When the phase transition takes place, bond orders change. As a consequence, VB experiences the broadening of some energy levels and the narrowing of others.

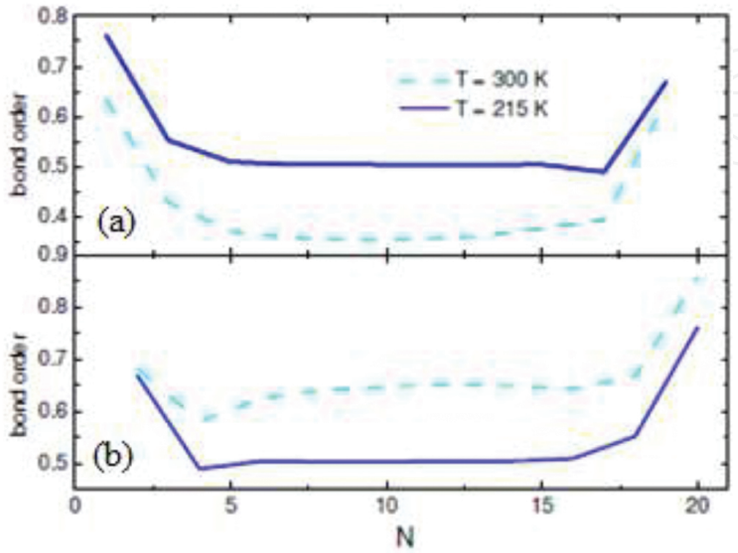

Figure 18. Bond orders between the atoms Sb3–S4 (a) and Sb4–S3 (b) along the SbSI molecular cluster in AFEP and FEP.

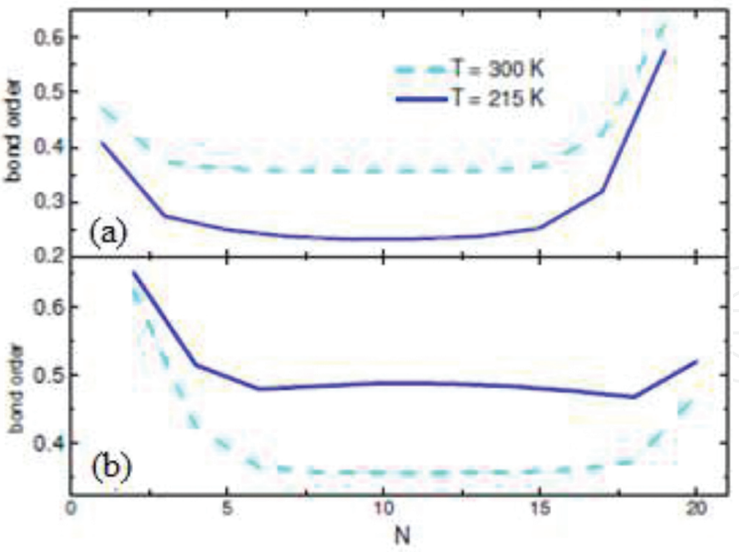

Figure 19. Bond orders between the atoms Sb3–I1 (a) and Sb4–I2 (b) along the SbSI molecular cluster in AFEP and FEP.

While the temperature decreases further in the FEP, Sb and S atoms change their positions relative to I atoms, and VB becomes broader. In Grigas et al. [39], the authors present the X-ray photoelectron spectra (XPS) of the VB and CL of the SbSI single crystals. The XPS are

measured in the energy range 0–1400 eV and the temperature range 130–330 K. They compared experimentally obtained energies of CL with the results of theoretical *ab initio* calculations. However, the experimentally obtained energies of the VB were not compared with the results of theoretical *ab initio* calculations.

We have calculated the density of states of VB for Sb, S, and I atoms and the total molecular cluster in AFEP (T = 300 K) and FEP (T = 215 K). The density of states is

$$g = \frac{\Delta N}{\Delta E},$$

where ΔN is the number of states in the energy interval ΔE (eV). The dimension of g is (eV^{-1}). In **Figure 20**, the experimental results of XPS VB spectra of SbSI crystals are compared with the theoretically calculated total density of states of a molecular cluster that consists of 20 SbSI molecules in AFEP (T = 300 K) and FEP (T = 215 K) is the number of states in the energy interval ΔE (eV). The dimension of g is (eV^{-1}). In **Figure 19**, the experimental results of XPS VB spectra of SbSI crystals are compared with the theoretically calculated total density of states of a molecular cluster that consists of 20 SbSI molecules in AFEP (T = 300 K) and FEP (T = 215 K). The average total density of states is as follows:

$$< g > = \frac{1}{n}\sum_i^n g_i,$$

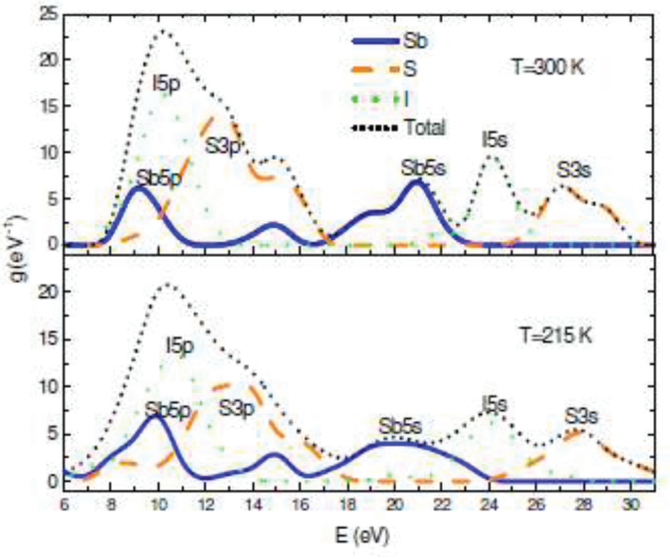

Figure 20. Theoretical total density of states of SbSI molecular cluster and density of states of Sb, S, and I atoms in AFEP and FEP.

where n is the number of normal modes (n = 15).

http://dx.doi.org/10.5772/64223

As seen from **Figures 20** and **21**, the experimental and theoretical results in AFEP and FEP are in good agreement in the energy range of 6–17 eV. In the range of 17–22 eV, there is a great difference between experimental and theoretical results.

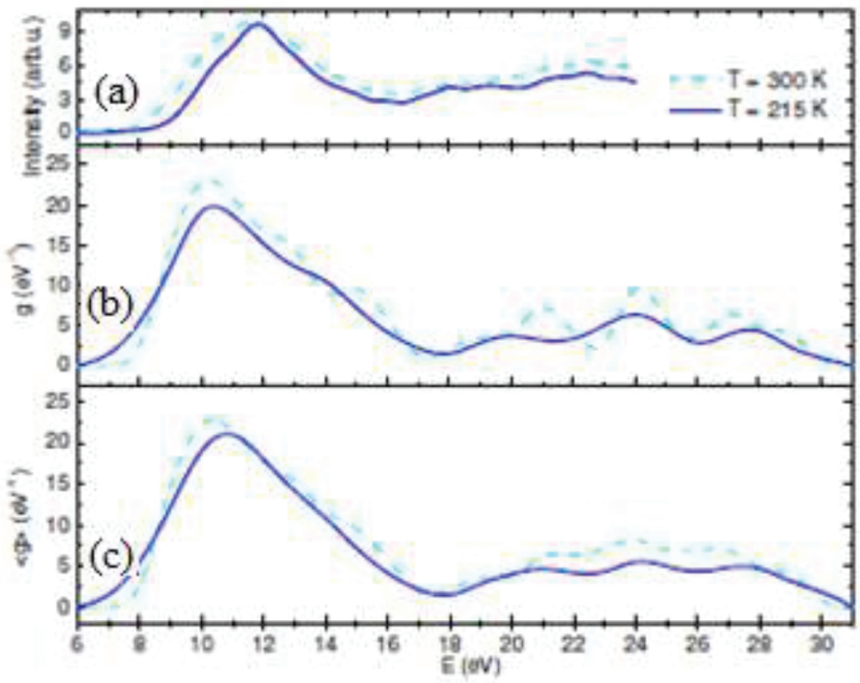

Figure 21. XPS of the VB of SbSI crystals in AFEP and FEP [13] (a). Theoretical total density of states (g) of SbSI molecular cluster in AFEP and FEP (b). The averaged total density of states (g) at molecular cluster when all atoms participate of oscillations of all normal modes (c).

The peaks of **Figures 21(a)** and **(b)** have no distinct shape in the XPS (at T = 300 K). This difference is explicable because the theoretical calculation does not take into account vibrational displacements of atoms. Average densities of states shown in **Figure 21(c)** are more similar to the experimental XPS spectrum than those from **Figure 21(b)**. Comparison of **Figures 20** and **21** shows the contribution of atomic states to the total density of states.

13. Core-level splitting in the antiferroelectric and ferroelectric phases

The mechanisms of the XPS splitting in SbSI crystals were discussed by Grigas et al. [39]. After the breaking of the crystals under high vacuum conditions some bonds of atoms (see **Figure 15b**) at the surface become open.

Employing the UHF method [40], the energy of CL and ionic charges of atoms Sb and S were calculated using the SbSI molecular cluster model. **Figure 22** demonstrates the calculated ionic charges of atoms Sb and S along a molecular cluster of 20 SbSI molecules.

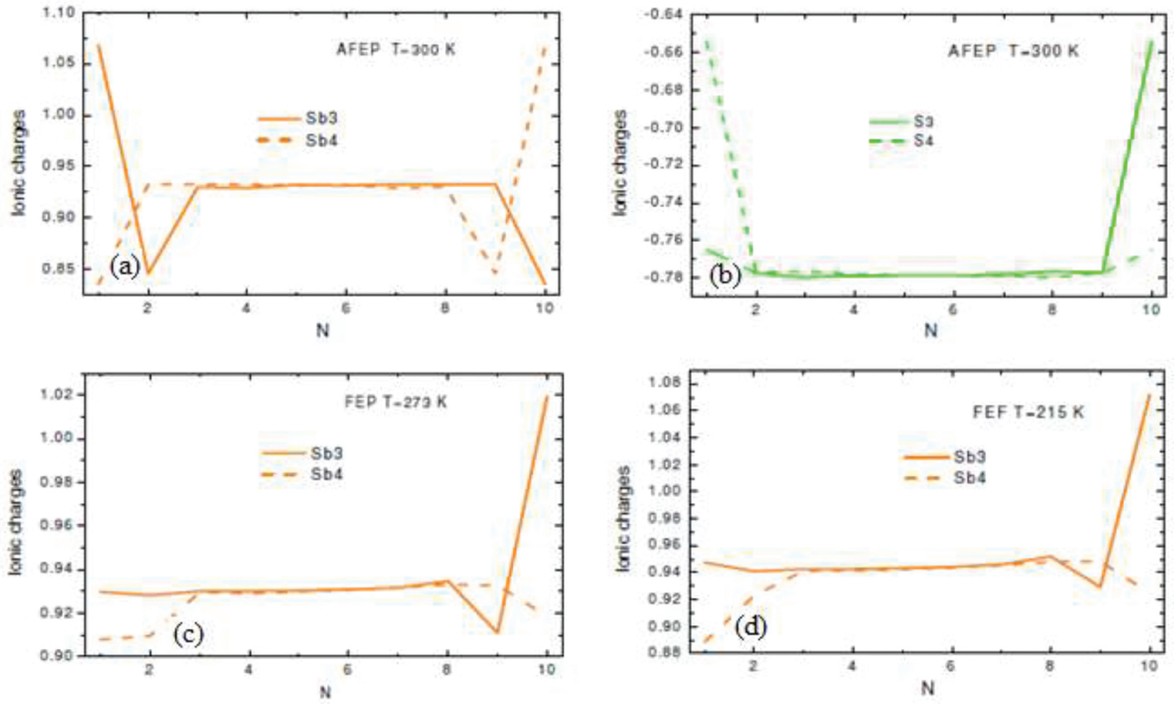

Figure 22. Ionic charges q of atoms Sb (a) and S (b) along SbSI molecular cluster in AFEP (T = 300 K). Ionic charges q of atoms Sb in FEP: T = 273 K (c) and T = 215 K (d).

As it is seen from **Figures 22(a)** and **(b)**, the ionic charges at the edges of the SbSI cluster in AFEP considerably differ from those in the bulk of the sample. Besides, the differences of charges Δq_i between Sb3 and Sb4 and between S3 and S4 have increased at the cluster edges. The differences of Sb3 and Sb4 are equal at both edges in AFEP and unequal in FEP.

The difference of charge Δq_i at the cluster edges forms the binding energy difference ($\Delta E_{clust} = E_{max} - E_{min}$) between atoms Sb3 and Sb4, S3 and S4, as well as I1 and I2 (**Table 9**). Moreover, the differences ($\Delta E_{clust} = E_{max} - E_{min}$) at both cluster edges are equal in AFEP and unequal in FEP.

State	Energy (eV)	State	Energy (eV)	State	Energy (eV)
Sb 3d	562.41	S 2p	180.54	I 3d	657.86
Sb^{+1} 3d	571.97	S^{-1} 2p	169.58	I^{-1} 3d	649.00
Sb^{+2} 3d	58,175	S^{-2} 2p	160.23		
Sb^{+3} 3d	593.13				

Table 10. The energies of CL of isolated neutral Sb, S, and I atoms and isolated Sb^{+1}, Sb^{+2}, Sb^{+3}, S^{-1}, S^{-2}, and I^{-1} ions.

Pursuing to explain the splitting of the CL, the eigenvalues of isolated neutral Sb, S, and I atoms and isolated Sb^{+1}, Sb^{+2}, Sb^{+3}, S^{-1}, S^{-2}, and I^{-1} ions have been calculated by the Hartree-Fock method using the *N21* orbital basis set (**Table 10**).

As shown in **Table 10**, the eigenvalues of isolated neutral atoms Sb and S and isolated ions Sb^{+1} and S^{-1} differ for all states. Besides, as demonstrated in **Table 10**, 3d state energies of an isolated Sb atom and Sb^{+1} ion vary by $\Delta E = 9.6$ eV. The difference for 2p states of S and S^{-1} makes $\Delta E = 11$ eV. Consequently, ΔE is proportional to ion charges Δq_i. The ion charges at the edge of the SbSI cluster vary between two Sb4 (and between two Sb3) by $\Delta q_i = 0.23$ a.u. and by $\Delta q_i = 0.18$ a.u. between two S4 (and between two S3; **Figure 22**). Hence, the energy difference ΔE^*_{clust} of the 3d state between two Sb atoms and of the 2p state between two S atoms at the edges of an SbSI cluster can be calculated as follows:

$$\Delta E^*_{clust} = \frac{\Delta q_i}{q_i} \Delta E \tag{32}$$

where ΔE is the difference between energies and q_i is the difference between ionic charges of isolated atoms (**Table 10**).

The proportion between ΔE^*_{clust} and Δq_i according to Eq. (33) allows us to explain the splitting, ΔE_{exp}, of the CL in XPS. So in AFEP XPS along the ***c***-axis, ΔE^*_{clust} and Δq_i are equal at both edges of the cluster (**Figures 22a** and **b**). However, in FEP their values are different. At phase transition, ΔE^*_{clust} changes differently at the left and right edges of the cluster (**Figures 22c** and **d**). Thus, at the left edge ΔE^*_{clust} (AFEP) > ΔE^*_{clust} (FEP) and at the right edge ΔE^*_{clust} (AFEP) < ΔE^*_{clust} (FEP). On the other hand, ΔE^*_{clust} is in good agreement with the difference $\Delta E_{clust} = E_{max} - E_{min}$ of the same CL energies of atoms at the edges of the cluster. For example, from **Table 4** we get $\Delta E_{clust} = 1.93$ eV between 3d of Sb3 and Sb4, 2.77 eV between 3d of I1 and I2, and 1.88 eV between 3d of S3 and S4 in AFEP (**Table 11**).

State	ΔE (eV) of isolated neutral atoms and ions with $q_i = 1$ (a.u.)	Δq_i (a.u.) of surface atoms of SbSI cluster	ΔE^*_{clus} (eV)	$\Delta E_{clus} = E_{max} - E_{min}$ (from Table 1) (eV)	ΔE_{exp} (eV)
Sb 3d	9.55	0.23	2.20	1.93	2.50
S 2p	11.51	0.18	2.07	1.88	2.20
I 3d	8.85	0.25	2.21	2.77	2.70

Table 11. The calculated splitting of the deep CL ΔE^*_{clust} and ΔE_{clust} in SbSI cluster and experimentally observed ΔE_{exp} of XPS levels in SbSI crystal.

As it is shown in **Table 11**, the experimentally observed ΔE_{exp} of the XPS levels in an SbSI crystal is in good agreement with the calculated splitting of the deep CL ΔE^*_{clust} and ΔE_{clust} in an SbSI cluster. Thus, it can be concluded that both Δq_i and ΔE_{clust} and the splitting of CL in an SbSI crystal are sensitive to the displacements of equilibrium position z_0 (depending on the temperature change).

14. The energy gap of the SbSI crystals

14.1. Introduction

Investigation of the total density of states of SbSI crystals [41] has shown that the absolute valence band top is formed in both phases of 3p orbitals of S, while the absolute conduction band bottom of 5p orbitals of Sb.

We have undertaken an attempt of a more detailed calculation of the electronic structure and some properties of SbSI from the first principles using the empirical pseudopotential method [42]. The method for calculating the band structure of SbSI was employed in Refs. [43–45]. In Ref. [43], purely ionic and partially covalent models were applied, and an indirect energy gap of 2.28 eV at point S was obtained. Nevertheless, the accuracy turned out to be 0.2 eV. In Ref. [44], the pseudopotentials were corrected applying the data on direct gaps. The absorption band edge in the paraelectric phase was determined at 1.82 eV for $\boldsymbol{E} \parallel \boldsymbol{c}$ $\left(S_{5\text{-}6}^{(V)} \rightarrow S_{7\text{-}8}^{(C)}\right)$ and 1.91 eV for $\boldsymbol{E} \perp \boldsymbol{c}$ $\left(S_{1\text{-}2}^{(V)} \rightarrow S_{7\text{-}8}^{(C)}\right)$. The valence band top corresponded to $S_{5\text{-}6}^{(V)}$, whereas the conduction band edge complied with $Z_1^{(C)}$ withthe energy of indirect gap of 1.41 eV. The energy gap sides matched to points Z and R in the ferroelectric phase. Analyzing the light reflection spectra, the indirect band gap of 1.82 eV between $\Gamma_6^{(V)}$ and $S_1^{(V)}$, as well as the minimum direct gap of 2.08 eV were obtained in reference [45].

In Ref. [45], a purely ionic model was assumed. The form factors of the pseudopotential were adjusted by fitting the calculated band gap values to the ones obtained both experimentally and theoretically by other authors. Form factors for Cl^- were used instead of I^-.

15. Investigation by using the pseudopotential method

The infinite crystal approximation, which states that the crystal properties obtained for the primary cell are extended then to the entire crystal employing periodical boundary conditions, has been employed. Hence, within the primary cell, the position of the *j*th atom of kind α(α = Sb, S, or I) is

$$\mathbf{R}_j^{(\alpha)} = \mathbf{R}_{\text{cell}} + \boldsymbol{\tau}_j^{(\alpha)}, \tag{33}$$

where $\mathbf{R}_{\text{cell}}$ is the translation vector of the orthorhombic system. The vectors $\tau_j^{(\alpha)}$ describe onprimitive translations that may be written as

$$\boldsymbol{\tau}_j^{\alpha} = \lambda_j^{\alpha} \boldsymbol{t}_x + \mu_j^{\alpha} \boldsymbol{t}_y + \nu_j^{\alpha} \boldsymbol{t}_z, \tag{34}$$

http://dx.doi.org/10.5772/64223

where t_x, t_y, and t_z are the lattice parameters along the three coordinate axes. The pseudopotential of the crystal has been selected as a sum of atomic pseudopotentials:

$$V(\mathbf{r}) = \mathbf{R}_{\text{cell}} \sum \alpha \quad \sum_{\mathbf{R}_{\text{cell}}} \quad \sum_j \nu_\alpha \left(\mathbf{r} - \mathbf{R}_{\text{cell}} - \boldsymbol{\tau}_j^{(\alpha)} \right). \tag{35}$$

Here, $\nu_\alpha(\mathbf{r})$ is the atomic pseudopotential of atom α. It is assumed to be localized and energy independent. Weakness of the pseudopotential $V^{ps}(\mathbf{r})$ provides good convergence of the pseudo-wave functions expanded in terms of plane waves:

$$\Psi_{\mathbf{k}i}^{\text{ps}}(\mathbf{r}) = \sum_G C_{\mathbf{k}i}(\mathbf{G}) \mathrm{e}^{\mathrm{i}(\mathbf{k}+\mathbf{G})\mathbf{r}}, \tag{36}$$

where $\mathbf{G}$ is the reciprocal lattice vector, $C_{\mathbf{k}i}(\mathbf{G})$ are Fourier coefficients. The Schrödinger equation in the pseudopotential method has the form

$$\left(H + V^{ps} \right) \Psi_{\mathbf{k}i}^{\text{ps}} = E_{\mathbf{k}i} \Psi_{\mathbf{k}i}^{\text{ps}}. \tag{37}$$

The pseudo-wave functions of the valence electrons $\Psi_{\mathbf{k}i}^{\text{ps}}(\mathbf{r})$ approach the true ones outside the core region, though they show no oscillations within the core. The Fourier component of this potential (or the matrix element in the plane-wave basis set) is expressed

$$V(\mathbf{G}) = \sum_\alpha S_\alpha(\mathbf{G}) \underset{\text{c}}{\overset{\alpha}{—}} \nu_\alpha(\mathbf{G}), \tag{38}$$

where Ω_α and Ω_c are the volume of the corresponding atom and of the primary cell as a whole. The atomic structural factor $S_\alpha(\mathbf{G})$ and atomic form factor $\nu_\alpha(\mathbf{G})$ are defined as

$$S_\alpha(\mathbf{G}) = \sum_\alpha e^{-\mathrm{i}\mathbf{G}\boldsymbol{\tau}_j(\alpha)}, \tag{39}$$

$$\nu_\alpha(\mathbf{G}) = \frac{1}{\Omega_\alpha} \int \nu_\alpha(\mathbf{r}) e^{-i\mathbf{G}\mathbf{r}} \mathrm{d}^3\mathbf{r} \tag{40}$$

The integrals are taken over the whole volume Ω_α. Provided the atomic coordinates within the cell are known, the atomic structural factor can be readily evaluated. The pseudopotential forms factors for Sb, S, and I, so the following equation [39, 43] was preliminary determined to be used:

$$v_{\alpha}(\mathbf{G}) = \frac{4\pi}{{}_{\alpha}|\mathbf{G}|^{-2}} \sum_{nlm} nlm \left| \exp\left[-i(\mathbf{Gr})\right] \right| nlm. \tag{41}$$

where *nlm* denotes the set of electron quantum numbers. Neutral functions for Sb, S, and I were involved by the numerical evaluation of the form factors [43, 45, 46]. It is significant that the agreement between the theoretical and experimental data shall be obtained solely employing neutral functions. It is noteworthy that some other authors [47, 48], who theoretically studied the band structure of the SbSI crystal, employed an ionic model of chemical bonding (Sb^{+3} S^{-2} I^{-1}) instead.

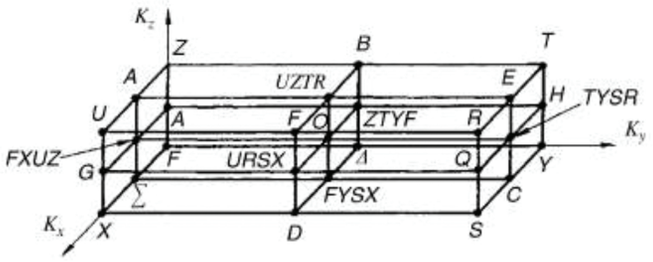

Figure 23. The scheme and notation of 27 special points in the irreducible part of the Brillouin zone.

No	Point	Coordinates		
		kx	*ky*	*kz*
1	Γ	0	0	0
2	Δ	0	0.25	0
3	Y	0	0.5	0
4	Λ	0	0	0.25
5	ZTY Γ	0	0.25	0.25
6	H	0	0.5	0.25
7	Z	0	0	0.5
8	B	0	0.25	0.5
9	T	0	0.5	0.5
10	Σ	0.25	0	0
11	ΓYSX	0.25	0.25	0
12	C	0.25	0.5	0
13	ΓXUZ	0.25	0	0.25
14	O	0.25	0.25	0.25
15	TYSR	0.25	0.5	0.25

No	Point	Coordinates		
		kx	*ky*	*kz*
16	A	0.25	0	0.5
17	ZTRU	0.25	0.25	0.5
18	E	0.5	0.5	0.5
19	X	0.5	0	0
20	D	0.5	0.25	0
21	S	0.5	0.5	0
22	G	0.5	0	0.25
23	URSX	0.5	0.25	0.25
24	Q	0.5	0.5	0.25
25	U	0.5	0	0.5
26	F	0.5	0.25	0.5
27	R	0.5	0.5	0.5

Table 12. Coordinates of the special points in the irreducible part of the Brillouin zone of SbSI (in relative units), see also **Figure 23**.

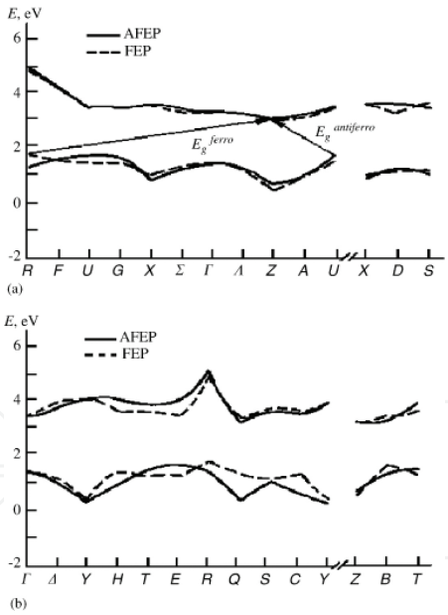

Figure 24. A diagram of the forbidden gap of SbSI in antiferroelectric phase at 308 K and its change after transition to ferroelectric phase (at 278 K). $E_g^{antiferro}$ in the indirect transition energy (1.42 eV) in antiferroelectric phase between points *U* and *Z* of the irreducible part of the Brillouin zone. $E_g^{antiferro}$ is the indirect transition energy (1.36 eV) in ferroelectric phase between points *R* and *Z* of the irreducible part of the Brillouin zone. The direct gap takes its minimum value at point *U* for both phases (a) and (b) correspond to different directions in the crystal.

The chemical bond in SbSI is of mixed kind, with contributions of both ionic and covalent components. As we have demonstrated in Ref. [43], it may be described by an approximate model formula $Sb^{+0.3}S^{-0.2}I^{-0.1}$. The band structure for both phases was estimated in 27 points of the irreducible part of the eightfold Brillouin zone, which is the total of 216 points over the Brillouin zone. The points are schematically described in **Figure 23**, as well as their coordinates are provided in **Table 12**. A total of 600 plane waves were included in the basis set for the calculation. The experimental energy gap values were estimated from the exponential light absorption tail at $\ln K = 6$, where K represented the absorption coefficient [2]. As it is seen from **Figure 24**, the most significant changes in the valence band at the phase transition occur at points Q and C (energy variation was 0.92 and 0.86 eV, respectively).

Moreover, the changes at points R (0.37 eV), H (0.55 eV), and E (0.42 eV) should be noted. As far as the conduction band is concerned, similar significant changes occur at points H (0.53 eV) and E (0.51 eV). At all the remaining points of the Brillouin zone, the band gap profile has changed insignificantly. All these changes have only a slight effect on the main characteristics of the band structure (except point R, obviously). As it is seen from **Figure 24**, the SbSI crystal has an indirect forbidden gap both in antiferroelectric phase and in ferroelectric phase [42]. The conduction band bottom in both phases is located at point $Z_1^{(C)}$, the valence band top in antiferroelectric phase is at the point $U_{5\text{-}6}^{(V)}$, and in ferroelectric phase at $R_{3\text{-}4}^{(V)}$. Our experimental and theoretical results of the SbSI crystal electronic structure sometimes differ from those obtained by other authors.

16. Band structure at the first-order phase transition

Direct (Brillouin zone point U) and indirect (jump $U \rightarrow Z$) dependence of the forbidden band on the temperature that has been calculated by us is demonstrated in **Figure 25**. As shown in **Figures 25** and **26**, the width of the indirect forbidden band is 1.42 eV in antiferroelectric phase and 1.36 eV in ferroelectric phase. The following results match well to the results that have been obtained earlier [49]: 1.42 eV in antiferroelectric and 1.36 eV in ferroelectric phase. The indirect width of the forbidden band is 1.36 eV in that band structure, which was obtained by moving to the point of phase transition from ferroelectric phase point B1; and it is 1.41 eV when moving from antiferroelectric phase point A1. Hence, the indirect forbidden band moving from antiferroelectric to ferroelectric phase alters by 0.05 eV, according to our calculations. This number complies with the change 0.06 eV of the width of the indirect band, which has been experimentally set [48, 49]. **Figures 3** and **4** reveal that the direct forbidden band is narrowest in point U, 1.83 eV. The calculations presented in Ref. [49] demonstrate the value of 1.82 eV. The minimal direct forbidden band in ferroelectric phase occurs in point G, 1.94 eV, whereas this gap is 1.98 eV in point U. The narrowest forbidden band is in point U of Brillouin zone, approaching from both antiferroelectric and ferroelectric sides. This has been estimated in band structure in the area of phase transition (**Figures 26b** and **c**). In the first case, it turned out to be1.83 eV, point A2 (**Figure 25**), and in the second one it is 1.87 eV, point B2 [43] (Figure 25). For this reason, the observed jump of the direct forbidden band is 0.04 eV during

the first-order phase transition. The change of the grating parameter along axis $c(y)$, which affects the band structure of SbSI crystal, causes this jump. It is possible to find the width of the forbidden direct band in Brillouin zone point U in Ref. [49, 50], which is experimentally measured. Unfortunately, the SbSI exponential edge of absorption has not been taken into account. The exponential edge of absorption is explored in greater detail in antiferroelectric and ferroelectric phases and in the area of the temperatures in the phase transition in Ref. [34]. The edge of the absorption in antiferroelectric phase complies with the Urbach's rule:

$$K = K_0 \exp\left[\frac{\sigma(E_K - E_0)}{kT}\right], \tag{42}$$

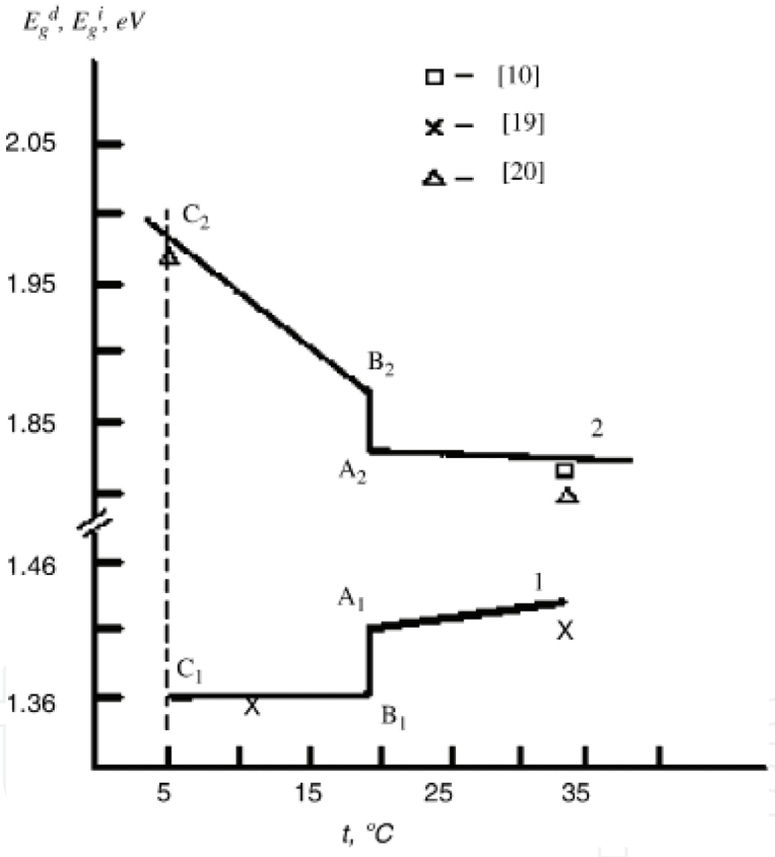

Figure 25. We got the direct (2) and the indirect (1) forbidden band width's dependence on temperature. The brake of the curve in points *A*1 and *A*2 is got when moving to phase transition from antiferroelectric phase, and in points *B*1 and *B*2 when moving to phase transition from ferroelectric phase.

here

$$\sigma = \sigma_0 \frac{2kT}{\omega_0} \text{th} \frac{\omega_0}{2kT}, \tag{43}$$

where σ stand for Urbach's parameter, which denotes the outspread of the absorption edge. The σ_0 is a constant, which describes the intensity of interaction between electrons and phonons, $\hbar\omega_0$ denotes effective phonons energy, K_0 denotes "oscillator's strength" or the maximal absorption coefficient, E_0 represents characteristic "gap" of the forbidden band, and E_K denotes light quantum energy for a particular absorption coefficient K. During the phase transition, the characteristic "gap" differs:

$$\Delta E_0 = E_{0\mathrm{F}} - E_{0\mathrm{AF}}, \tag{44}$$

where $E_{0\mathrm{F}}$ and $E_{0\mathrm{AF}}$ stand for the values of the energy "gap" in ferroelectric (F) and antiferroelectric (AF) phases, respectively. As seen from Eq. (43), temperature dependences $E_\mathrm{K}(T)$ and σ/kT (T) should be measured when K = const. and K_0 (T) in both phases in the area of the phase transition in order to determine $E_{0\mathrm{F}}$ and $E_{0\mathrm{AF}}$. K_0 (T) is not temperature dependent in antiferroelectric phase and it is experimentally defined. Different temperatures are matched finding the point of crossing of the curve ln$K$ (E). In ferroelectric phase, $K_{0\mathrm{F}}$ is determined as follows:

$$\ln K_{0\mathrm{F}} = \ln K_0 - \gamma\left(\frac{\sigma}{kT}\right)_{\mathrm{AF}} P_\mathrm{S}^2, \tag{45}$$

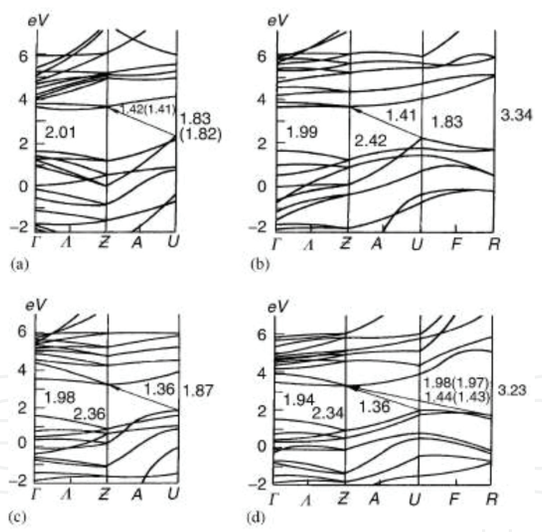

Figure 26. The band structure of SbSI monocrystal: (a) in antiferroelectric phase (T = 308 K), (b) in points of phase transition moving from antiferroelectric phase (**Figure 25** points $A1$ and $A2$; T_C = 295 K), (c) in points of phase transition moving from ferroelectric phase (**Figure 25** points $B1$ and $B2$; T_C = 295 K), and (d) in ferroelectric phase (**Figure 25** points $C1$ and $C2$; T = 278 K). Arrows show the width of the forbidden indirect band.

where lnK_0 and $(\sigma/kT)_{\mathrm{AF}}$ are the parameters in the antiferroelectric phase, and γ represents the coefficient of proportionality (polarization potential). It is possible to find the values of γ, K_0, P_S (T) and Eq. (42) in Ref. [34]. **Figure 27** demonstrates temperature dependencies of E_K (T) and σ/kT (T), which have been measured experimentally employing the dynamic method with a

continuously variable temperature [51]. Using experimental results provided in **Figure 27**, when temperature is 295 and 278 K, as well as employing the data indicated in Ref. [34], we estimate that according to Eqs. (43) and (46), $\Delta E_0 = 0.12 \pm 0.02$ eV. The experimental ΔE_0 value coincides with the theoretic variation of the width of the forbidden band in margins of error, which is 0.11 eV in Brillouin zone point U. It appears due to the variation of the grating parameters along the axis $c(y)$, which affects the band structure of crystal (**Figures 26c** and **d**).

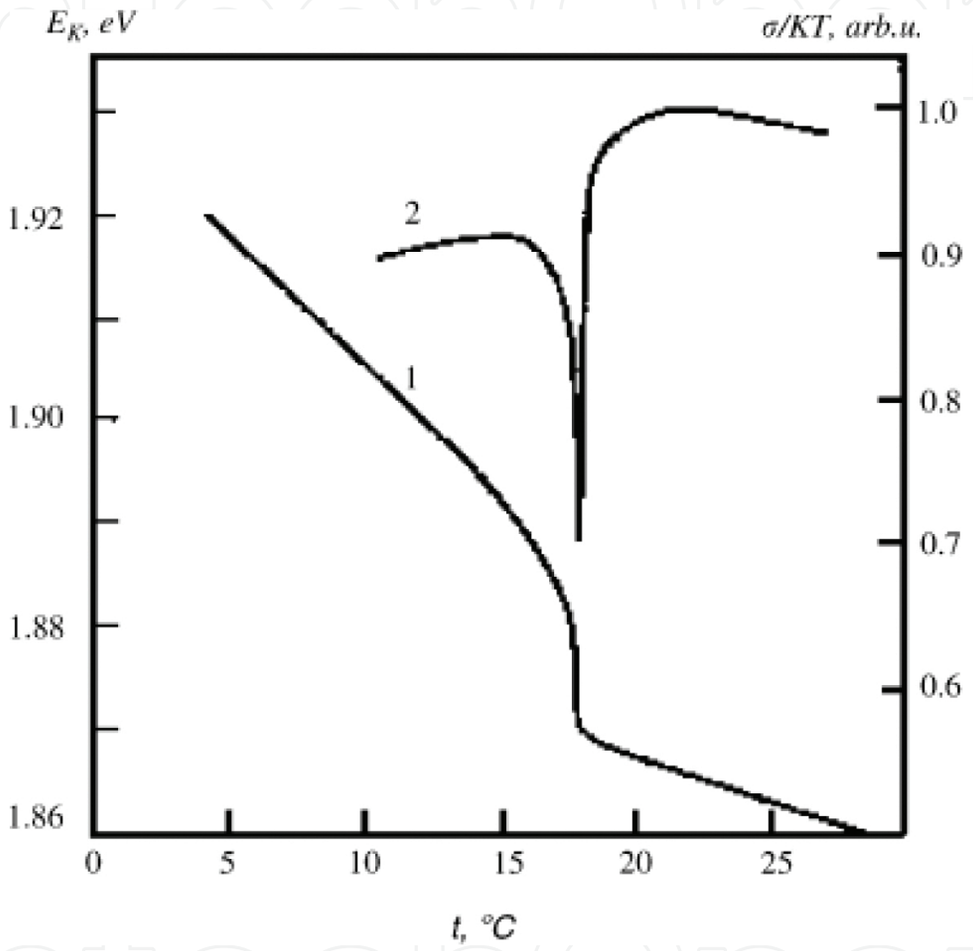

Figure 27. The experimental izo absorption curve energy E_K (eV) dependence on temperature when $K = 65$ cm^{-1} (1) and the dependence σ/kT (T) (2) are measured in SbSI at phase transition.

17. Conclusions

The potential energy of $A_u(10)$, $B_{1u}(3)$, $B_{2g}(4)$, $B_{2g}(5)$, and $B_{3g}(7)$ normal modes in the paraelectric phase are anharmonic with a double-well $V(z)$, while $B_{1u}(2)$, $B_{2g}(6)$, $B_{3g}(8)$, and $B_{3g}(9)$ modes possess only one minimum. The semisoft modes $B_{1u}(3) \rightarrow \boldsymbol{A_1}$, $B_{2g}(4) \rightarrow \boldsymbol{B_1}$, $B_{2g}(5) \rightarrow \boldsymbol{B_1}$, and $B_{3g}(7) \rightarrow \boldsymbol{B_2}$ evoke experimental reflection $R(k)$ peaks for $\boldsymbol{E} \| \boldsymbol{c}$ in the range of $k = 10$–100 cm^{-1} for both paraelectric and ferroelectric phases. The $R(k)$ peak for $\boldsymbol{E} \| \boldsymbol{c}$ in the paraelectric phase

is created by mode $B_{1u}(2)$, but in the ferroelectric phase the $R(k)$ peaks are caused by modes $B_{1u}(2) \rightarrow \boldsymbol{A_1}$, $B_{2g}(6) \rightarrow \boldsymbol{B_1}$, $B_{3g}(8) \rightarrow \boldsymbol{B_2}$, and $B_{3g}(9) \rightarrow \boldsymbol{B_2}$. It has been determined that strong lattice anharmonisity, as well as interaction between chains, can split the mode $B_{1u}(3)$ into two components, from which one is soft in the microwave range and the other $B_{1u}(3)$ is semisoft in the *IR* range. The semisoft modes $B_{1u}(3)$, $B_{2g}(4)$, $B_{2g}(5)$, and $B_{3g}(7)$ increase the large (absorption) peak in the range k = 5–100 cm^{-1} and the dielectric contribution of $\Delta\varepsilon \approx 5000$. The reflection spectra also show large peaks due to its strong temperature dependence. The strongest temperature dependence of reflection is observed in the ferroelectric phase. While in the paraelectric phase it becomes relatively weak.

In the long SbSI chains, the highest levels of one-electron energies in the valence band top are degenerate. Therefore, Jahn-Teller effect appears as an important factor. The ferroelectric phase transition in SbSI crystals is caused by electron-phonon and phonon-phonon interactions. The electron-phonon interaction reduce harmonic coefficient K, whereas phonon-phonon interaction reverses its sign, i.e., $K < 0$; $c > 0$. In the phase transition region, anomalous behavior is demonstrated by the coefficients of the polynomial expansion of the total energy E_T dependence upon the $_u$ normal mode coordinate. The $_u$ mode temperature dependence of the coefficient $K = m_\tau^2$ is similar to the temperature dependence of the soft mode frequency, ω_s^2.

Acknowledgements

This works was supported by Science Foundation from Lithuanian University of Educational Sciences.

Author details

Algirdas Audzijonis, Leonardas Žigas*, Raimundas Sereika and Raimundas Žaltauskas

*Address all correspondence to: leonardas.zigas@leu.lt

Faculty of Science and Technology, Lithuanian University of Educational Sciences, Vilnius, Lithuania

References

[1] E. Fatuzo, G. Harbeke, W. J. Merz, Nitsche, H. Roetschi, and W. Ruppel, Ferroelectricity in SbSI, *Phys. Rev.* 1962, 127, 2036–2037.

[2] E. I. Gerzanich and V. M. Fridkin, Dependence of dielectric properties of SbSI on temperature and on hydrostatic pressure, *Solid State Phys.* 1968, 10, 3111–3113.

[3] A. Audzijonis, S. Kvedaravičius,V. Paulikas, J. Siroicas, N. Mykolaitienė, and R. Šadžius, Origin of optical anomalies in the ferroelectric phase transition region of SbSI and SbSBr crystals, *Ferroelectrics* 1998, 215, 221–231.

[4] A. Audzijonis, R. Žaltauskas, L. Audzijonienė I. Vinokurova, O. Farberovich, and R. Šadžius, Electronic band structure of ferroelectric semiconductor SbSI studied by empirical pseudopotential, *Ferroelectrics* 1998, 211, 111–126.

[5] A. Audzijonis, R. Žaltauskas, I. V. Vinokurova, O. V. Farberovich, and R. Šadžius, Variation of the SbSI crystals energy gap at phase transition, *Ferroelectrics* 1998, 209, 505–515.

[6] J. Petzelt, Far infrared reflectivity of SbSI, *Phys. Stat. Sol.* (b) 1969, 36, 321–333.

[7] F. Sugawara and T. Nakamura, Far-infrared reflectivity spectra of KH_2PO_4 crystal, *J. Phys. Soc. Jpn.* 1970, 28, 158–160.

[8] F. Sugawara and T. Nakamura, Far-i.r. reflectivity spectra of SbSI. *J. Phys. Chem. Sol*. 1972, 33, 1665–1668.

[9] B. K. Agrawal and C. H. Perry, Long-wavelength optical phonons and phase transitions in SbSI, *Phys. Rev*. *B* 1971, 4, 1893–1902.

[10] A. Koutsodakis, I. Louizis, A. Bartzokas, and D. Siapkas, Far infrared reflectivity spectra of $A^{V}B^{VI}C^{VII}$ compounds, *Ferroelectrics* 1976, 12, 131–133.

[11] J. Grigas and R. Beliackas, Macrowave resonant dielectric dispersion in paraelectric phase of SbSI crystals, *Solid State Phys* 1978, 20, 2123–2125.

[12] V. Kalesinskas, J. Grigas, A. Audzijonis, and K. Žičkus, Microwave resonant dielectric dispersion in $SbS_{0.7}Se_{0.3}I$ crystals, *Phase Transit.* 1983, 3, 217–226.

[13] V. Kalesinskas, J. Grigas, R. Jankevičius, and A. Audzijonis, Soft mode in the microwave dielectric spectra of the SbSI-BiSI system, *Phys. Stat. Sol*. (b) 1983, 115, K11–K13.

[14] S. Kvedaravičius, A. Audzijonis, N. Mykolaitienė, and J. Grigas, Soft mode and its electronic potential in SbSI-type mixed crystals. *Ferroelectrics* 1996, 177, 181–190.

[15] A. Audzijonis, J. Grigas, A. Kajokas, S. Kvedaravičius, and V. Paulikas, Origin of ferroelectricity in SbSI, *Ferroelectrics* 1998, 219, 37–45.

[16] A. Audzijonis, L. Žigas, R. Žaltauskas, J. Narušis, and L. Audzijonienė, Electronic potentials of normal vibrational modes in SbSI crystals, *Ferroelectrics* 2002, 274, 1–15.

[17] K. Lukaszewicz, A. Pietraszko, J. Stepien-Damm, and A. Kajokas, Crystal structure and phase transitions of the ferroelectric antimony sulfoiodide SbSI. Part I. Phase diagram and thermal expansion of SbSI *Polish J. Chem*. 1997, 71, 1345-1349; Part II. Crystal Structure of SbSI in Phases I, II and III, 1852–1857.

[18] M. Balkanski, M. K. Teng, S. M. Shapiro, and M. R. Ziolkiewicz, Lattice modes and phase transition in SbSi, *Phys. Stat. Sol*. (b) 1971, 44, 355–368.

[19] K. R. Rao, S. L. Chaplot, V. M. Padmanarhan, and P. R. Vijayaraghavan, Neutron, X-ray and lattice dynamical studies of paraelectric Sb_2S_3, *Pramana* 1982, 19, 593–632.

[20] K. R. Rao and S. L. Chaplot, Dynamics of paraelectric and ferroelectric SbSI, *Phys. Stat. Sol*. (b) 1985,129, 471–482.

[21] M. Balkanski, M. K. Teng, and M. Nusimovici, Raman scattering in KNO_3 phases I, II, and III, *Phys. Rev*. 1968, 176, 1098–1106.

[22] L. Žigas, Vibration spectra of SbSI and Sb_2S_3 type crystals in region of phase transition, *Vilnius* 2001, 134.

[23] E. Furman, O. Brafman, and J. Makovsky, Approximation to long-wavelength lattice dynamics of SbSI-type crystals, *Phys. Rev*. B 1976, 13, 1703–1710.

[24] J. Batarūnas, A. Audzijonis, N. Mykolaitiene, and K. Žičkus, The electronic potential of paraelectric SbSI, *Phys. Stat. Sol*. (b) 1988, 150, K31–K34.

[25] J. Grigas, Microwave dielectric spectroscopy of ferroelectrics and related materials, Gordon S Breach Publisher, OPA, Amsterdam, 1996, 336 p.

[26] A. R. Hutson, J. H. McFee, and D. L. White, Ultrasonic amplification in CdS, *Phys. Rev. Lett.* 1961, 7, 237–239.

[27] C. Scheiding and G. Schmidt, Piezoelectricity and electrostriction of SbSI single crystals, *Phys. Stat. Sol.*(a) 1972, 9, K77–K80.

[28] D. Berlincourt, H. Jaffe, W. J. Merz, and R. Nitsche, Piezoelectric effect in the ferroelectric range in SbSI, *Appl. Phys. Letters* 1964, 4, 61–65.

[29] A. Audzijonis, L. Žigas, J. Siroicas, J. Narušis, R. Žaltauskas, A. Pauliukas, A. Čerškus, and R. Šadžius, Investigation of the soft mode of $SbSBr_xI_{1-x}$ crystals, *Ferroelectrics* 2004, 300, 15–31.

[30] A. Audzijonis, G. Gaigalas, V. Lazauskas, L. Žigas, J. Narušis, and A. Pauliukas, Electron–phonon interaction and Jahn–Teller effect in the SbSI atomic chain, *Phys. B: Condens. Matter* 2004, 351, 27–34.

[31] N. Kristoffel and P. Konsin, Pseudo-Jahn-Teller effect and second order phase transitions in crystals, *Phys. Stat. Sol.* (b) 1967, 21, K39–K43.

[32] N. Kristoffel and P. Konsin, Displacive vibronic phase transitions in narrow-gap semiconductors, *Phys. Stat. Sol.* (b) 1968, 28, K731–K739.

[33] M. W. Schmidt, K. K. Baldridge, J. A. Boatz, S. T. Elbert, M. S. Gordon, J. H. Jensen, S. Koseki, N. Matsunaga, K. A. Nguyen, S. J. Su, T. L. Windus, M. Dupuis, and J. A. Montgomery, General atomic and molecular electronic structure system, *J. Comput. Chem*. 1993, 14, 1347–1363.

[34] K. Zickus, A. Audzijonis, J. Batarunas, and A. Sileika, The fundamental absorption edge tail of ferroelectric SbSI, *Phys. Stat. Sol.* (b) 125, 1984, 645–651.

[35] J. Petzelt, G. V. Kozlov, A. A. Volkov, Dielectric spectroscopy of paraelectric soft modes, *Ferroelectrics* 1987, 73, 101–123.

[36] E. I. Gerzanich and V. E. Fridkin, A*V* B*VI* C *VII* type Ferroelectrics, Nauka, Moskva 1982, 228 p.

[37] S. Kvedaravičius, A. Audzijonis, and N. Mykolaitienė, The electronic potential of SbSI crystal in the region of phase transition, *Ferroelectrics* 1993,150, 381–385.

[38] Y. V. Sukhetskii, A. V. Soldatov, A. N. Gusatinskii, K. Žičkus, and A. Audzijonis, Energy band structure of $SbS_xse_{1-x}I$, *Phys. Stat. Sol.* (b) 1985, 132, K103–K106.

[39] Y. Sukhetskii, A. Soldatov, V. Likhacheva, K. Žičkus, A. Audzijonis, and A. Gusatinskii, X-ray spectroscopic investigation of the energy band structure of SbSBr, *Lithuan. J. Phys.* 1986, 26, 31–36.

[40] J. Grigas, E. Talik, and V. Lazauskas, Splitting of the XPS in ferroelectric SbSI crystals, *Ferroelectrics* 2003, 284, 147–160.

[41] A. Audzijonis, G. Gaigalas, L. Žigas, J. Narušis, A. Pauliukas, R. Žaltauskas, and A. Čerškus, Splitting of the XPS in ferroelectric SbSBr crystals, *Ferroelectrics Lett.* 2005, 32, 111–118.

[42] I. V. Vinokurova, O. V. Farberovich, A. Audzijonis, and R. Žaltauskas, Optical properties of SbSI crystals in the phase transition region, *Lithuanian J. Phys.* 1995, 35, 306–113.

[43] A. Audzijonis, R. Žaltauskas, L. Žigas, I. V. Vinokurova, O. V. Farberovich, A. Pauliukas, and A. Kvedaravičius, Variation of the energy gap of the ferroelectric SbSI crystals at the phase transition, *Phys. B: Condens. Matter* 2006, 371, 68–73.

[44] I. F. Alward, C. Y. Fong, M. El-Batanonny, and F. Wooten, Electronic and optical properties of SbSBr, SbSI and SbSeI, *Solid State Commun.* 1978, 25, 307–310.

[45] M. L. Cohen and V. Heine, The fitting of pseudopotentials to experimental data and their subsequent application, in Solid State Physics, Vol. 24, eds. H. Ehrenreich, F. Seitz, and D. Turnbull, Academic Press, New York, 1970, 37 p.

[46] C. Y. Fong, Y. Petroff, S. Kohn, et al., Wavelength modulation spectra of SbSI, its electronic band structure, *Solid State Commun.* 1974, 14, 681–685.

[47] K. Nakao and M. Balkanski, Electronic band structures of SbSI in the para- and ferroelectric phases, *Phys. Rev.* B 1973, 8, 5759–5780.

[48] K. Žičkus, A. Audzijonis, J. Batarūnas, and V. Lazauskas, Chemical bond approach to the dielectric constant of SbSI, *Solid State Commun.* 1986, 60, 143–145.

[49] A. Audzijonis, K. Žičkus, J. Batarūnas, V. Lazauskas, N. Mykolaitienė, and J. Grigas, The chemical bond of $A^{V}B^{VI}C^{VII}$ crystals. In: Abstracts 6th International Meeting on Ferroelectricity, August 12, Kobe, Japan, 1985, 33 p.

[50] T. A. Pikka and V. M. Fridkin, Phase transitions in A^{V} B^{VI} C^{VII} type ferroelectrics-semiconductors, *Solid State Phys.* 1968, 10, 3378–3384.

[51] G. Harbeke, Absorption edge in ferroelectric SbSI under electric fields, *Phys. Chem. Sol.* 1963, 24 (N7), 957–963.